Topographic Response of a Harbor during a Meteotsunami in the Puerto Rican Archipelago

By

Edwin Alfonso-Sosa, Ph.D.

14-January-2015

Introduction

There is new evidence that Puerto Rico is frequently hit by meteotsunamis during August, when strong tropical waves come from the East accompanied by jumps in atmospheric pressure (Alfonso-Sosa, 2014). The term Meteotsunami is used to designate a series of waves in a harbor (bay) that show a similar frequency or amplitude to that of a tsunami generated by earthquakes, landslides or volcanic eruption, but unlike these, its origin is associated with an atmospheric disturbance able to generate a barotropic long wave in the open sea, and resonate with it (Proudman resonance) when approaches the coast. Once reaches the harbor (bay) is capable of forcing a number of waves, which enter in a second resonance with the harbor (bay) which amplifies it again. The meteotsunami only occurs in certain harbors (bays) where this double resonance is possible. These harbor oscillations are confined to the seiche band, whose limits are from 12 CPD to120 CPD. This study is focused to determine amplification (or topographic response) in 12 harbors (bays) of the Puerto Rican Archipelago. On August 16 2011, a meteotsunami was detected by 12 NOS water-level stations. This singular event presents us with the unique opportunity to analyze high quality water-level data; that allow us to calculate the harbor's amplification for many harbors in Puerto Rico. It is important to know the topographic response of the harbors (bays) of Puerto Rico; this way we can identify those locations where their oscillations (coastal seiches) will be larger or last longer. In these harbors marine activities will be affected the most. Coastal seiches are nonlinear and nonstationary phenomena analyzed using Hilbert-Huang Transform (HHT) analysis (Huang et. al., 2000). HHT analysis is more robust than Fourier analysis for this kind of oscillation. I hope this paper will inspire others to use this same approach.

Water Level Gauge (WLG) Data

Six days of verified 6-min water-level data recorded by an array of acoustic water-level gauges (WLGs) located in the Puerto Rican Archipelago (Figure 1) and operated by the National Ocean Service (NOS) were used for this study. The 6-day record goes from AUG-13-2011 00:00 GMT to AUG-18- 2011 23:54 GMT. The acoustic sensor (4 Hz) take measurements at 6-minute intervals with each measurement consisting of a set of 181 one-second interval water level samples centered on each tenth of an hour. The 181 samples are averaged, a three standard deviation outlier rejection test applied, and the mean and standard deviation recalculated and reported along with the number outliers. The reported measurements have 0.01 foot resolution and are stored in system memory. The data is available from the following NOAA/NOS/CO-OPS website: http://tidesandcurrents.noaa.gov/

Hilbert-Huang Transform (HHT) Analysis

In this paper we provide only a brief explanation of HHT analysis. It consists of a combination of Empirical Mode Decomposition (EMD) and Hilbert Spectrum Analysis (HSA). A detailed explanation can be found in Huang et al. (1998, 1999). The application of HHT for analyzing nonstationary and nonlinear geophysical series has been reported in a number of papers (Huang et al. 2001, Huang et al. 2000). HHT performs time-frequency analysis of nonstationary signals, as do other techniques such as wavelets (Huang et al. 1998). However, HHT is better suited than wavelets for analyzing signals resulting from nonlinear processes. This advantage motivated us to choose HHT to analyze our data. EMD can separate the signal into orthogonal components with different time scales.

HHT analysis starts with empirical mode decomposition (EMD). This technique decomposes time series data into a finite number of intrinsic mode functions (IMFs) with time variable amplitudes and frequencies. The decomposition is orthogonal and adaptive[1]. Any function is an IMF if (1) in the whole data set, the number of extrema and the number of zero-crossings is either equal of differ at most by one, and (2) at any point, the mean value of the envelope defined by the local maxima and the envelope defined by the local minima are zero. The second criterion means that the function has symmetric envelopes defined by local maxima and minima respectively. The process to achieve this decomposition is called “extrema sifting”. We limit the sifting to 100 times with a stoppage criterion of 20 times (CE(100,20), in the notation used by Huang, et al., 1998). This method allows us to (e.g.) easily separate the meteotsunami signal from the tidal components. An IMF is a band-limited signal which is amenable to the Hilbert transform. Hence, each IMF component can be expressed as an analytic signal:

$$c(t) = a(t)\exp(i\theta(t)), \qquad (1)$$

[1] By adaptive we mean that the EMD decomposition adapts to the local variations of the data. Adaptive basis is indispensable for nonstationary and nonlinear data analysis.

where $a(t)$ is the time varying amplitude and $\theta(t)$ is the time varying phase. These can be obtained from

$$a(t) = [X^2(t) + Y^2(t)]^{1/2}, \qquad \theta(t) = \arctan\left(\frac{Y(t)}{X(t)}\right) \tag{2}$$

X(t) and Y(t) represent the real and imaginary part of c(t), respectively. The imaginary part was defined by the Hilbert transform of the original signal, X(t).

$$Y(t) = \frac{1}{\pi} P \int_{-\infty}^{\infty} \frac{X(t')}{t - t'} dt', \tag{3}$$

where P indicates the Cauchy principal value. Y(t) is a version of the original real sequence with a 90° phase shift.

Variable $a(t)$ is the time varying amplitude of the analytic signal *c(t)*. It traces the envelope amplitude of the IMF component (Figure 3). $a^2(t)$ is then the relative energy of the modulation envelope.

The instantaneous frequency is defined as the time derivative of the instantaneous phase angle $\theta(t)$

$$\omega = \frac{d\theta}{dt}. \tag{4}$$

Once we have decomposed the original series *X(t)* into *L* IMFs and applied the Hilbert transform to each, we can represent the original series as

$$X(t) = \sum_{\lambda=1}^{L} c_\lambda(t) = \sum_{\lambda=1}^{L} a_\lambda(t) \exp(i \int \omega_\lambda(t)\, dt). \tag{5}$$

Using (1) and (4), we define the Hilbert amplitude spectrum as, $H_\lambda(\omega_\lambda(t), t) = a_\lambda(t)$ at $\omega_\lambda(t)$, for all modes λ. *H* is displayed as a contour plot in the time-frequency plane. Alternatively, using the square of *a(t)* results in the Hilbert energy spectrum. With the Hilbert spectrum defined, we can also define the marginal spectrum (Huang et al. 1998), h(ω), as

$$h(\omega) = \int_0^T H(\omega, t) \quad dt. \tag{6}$$

The marginal spectrum offers a measure of total amplitude (or energy) contribution from each frequency value. It represents the cumulated amplitude over the entire data span in a probabilistic sense. The spectral density is expressed in squared feet per cycle per day (ft^2/CPD).

The foregoing is a synopsis of the HHT method. Details can be found in the cited references.

Determining Harbor Amplification

The effect of topography on a *sea-level arrival series* recorded at the coastal WLG can be determined by comparing the *sea-level arrival marginal spectrum*, $h_a(\omega)$, with the *deep-water marginal spectrum*, $h_{dw}(\omega)$, via an amplification transfer function, $A^2(\omega)$,

$$h_a(\omega) = A^2(\omega) \quad h_{dw}(\omega) \tag{7}$$

then the harbor amplification function can be determined from the squared-root of the ratio between $h_a(\omega)$ and $h_{dw}(\omega)$,

$$A(\omega) = \sqrt{\frac{h_a(\omega)}{h_{dw}(\omega)}}. \tag{8}$$

A similar approach for quantifying the tendency of local topography to amplify the sea level variability was applied by Allen and Greenslade (2009). But their approach was based on Fourier spectral analysis. They applied it to Australian and South-West Pacific sea-level gauge records. This paper follows a stronger approach because it is based in HHT analysis, a powerful analysis method for nonlinear and nonstationary time series. The Fourier spectral analysis is less robust because it generates spurious harmonics that are an artifact and are not a real representation of the physical signal.

Gaussian Fit

From equation 8 we generated a distribution of harbor-amplitude values as a function of frequency. To discern the general form of the amplitude function we fitted it with the following Gaussian model:

The Gaussian model fits peaks, and is given by

$$y = \sum_{i=1}^{n} a_i \exp\left[-\left(\frac{x-b_i}{c_i}\right)^2\right]$$

where *a* is the amplitude, *b* is the centroid (location), *c* is related to the peak width, *n* is the number of peaks to fit, and $1 \le n \le 8$. In our case we limit the n-value to n=2 or n=3. For this work we used Matlab's Curve Fitting Application (cftool) applying a nonlinear least square method with two robust algorithms called LAR and Bisquare. We kept the default finite differencing parameters and convergence criteria.

Results

From Figure 2 to Figure 14 we show the empirical mode decomposition (EMD) analysis of the sea level data on each of the 13 WLG stations. Each panel of the figure shows the amplitude of the Intrinsic Mode Function (IMF) and each of them has physical meaning. In most of the figures, the fourth and fifth IMFs represent the semidiurnal and diurnal tides, respectively. The first, second, and third IMF contain all the variance associated with the meteotsunamis. All the amplitudes are expressed in feet and the time in GMT. The EMD analysis reveals two distinct meteotsunami events, one at the end of YD 228 and the second one at the start of YD 229. For case of Puerto de Fajardo, the first meteotsunami was at YD 228.7 and the second one occurred 8.2 hours later, on YD 229.1. The first meteotsunami was detected by all the WLG stations, but the second one was detected only by WLG stations located in the East side of the archipelago: Puerto de Naguabo, Puerto de Fajardo, Isabel Segunda, Culebra, and barely detectable in Esperanza. The first event showed larger amplitudes in the West side of the Main Island, in particular Bahia Salinas with 0.30 feet and Puerto Real with 0.24 feet. The second event showed larger amplitudes in Fajardo with 0.41 feet (combining the first three IMFs) and in Puerto de Naguabo with 0.24 feet. A more detailed description of the first meteotsunami event can be found in Alfonso-Sosa (2012) and for the second meteotsunami in Alfonso-Sosa (2014). Both papers provide a detailed explanation of the generation mechanism.

From Figure 16 to Figure 27 we show the sea-level arrival marginal spectrum, ha(ω), for each of the 13 WLG stations. By comparing all of them we found that the one from Crash Boat in Aguadilla (Figure 15) shows much less energy density in the seiche band (12 CPD - 120 CPD) than the rest of the stations. This is explained by the extremely short shelf length (~1.5 km). The narrow shelf cannot amplify the sea-level variability in the seiche band. The Crash Boat's marginal spectrum represents the deep-water variability better than any other. For this reason we select it as our deep-water marginal spectrum instead of choosing a theoretical deep-water spectrum. The real deep-water spectrum reduces the overestimation of the harbor amplification. Figure 28 and Figure 29 show the sea-level arrival marginal spectrum overlapping the deep-water marginal spectrum for two locations, Puerto Real and Bahia Salinas, respectively. Both figures reveal the amplification in the seiche band of the sea-level arrival marginal spectrum relative to the deep-water marginal spectrum.

Now by means of equation 8 we determined the topographic response in the seiche band (12 CPD - 120 CPD) for six ports and bays in the Puerto Rican Archipelago. We show only those localities where the amplification response was stronger: Bahia Salinas, Culebra, Puerto de Fajardo, Puerto de Isabel Segunda, Puerto de Naguabo y Puerto Real. Figures 30-35 show the topographic response of those harbors. Most of the harbor's amplification values are below 4 units but some reached up to 18 units. A practical way to compare each harbor's amplification distribution is by means of a Gaussian fit of it. These Gaussian curves can be easily compared, as it is shown in Figure 36. The curves show bimodal or

tri-modal form. For frequencies between 20.7 CPD and 24.5 CPD, the harbor amplification values ranged between 2.9 and 3.8 units; observed at Puerto Real, Puerto de Naguabo and Puerto de Fajardo (see table below Figure 36). For the previous harbors, on frequencies between 50.5 CPD and 54.4 CPD the amplitudes ranged between 2.5 and 3.9 units. In Bahia Salinas, the amplification reached 2.4 units at a higher frequency of 74.6 CPD. Average harbor amplitude from all peak amplitudes is 2.6 ± 0.7 units. Despite some similarities each harbor amplification curve is unique. The Gaussian curves are the best-fit of the harbor's amplifications and they reveal the general form of the harbor's topographic response.

Discussion

Our results showed the variety of topographic responses for some harbors and bays in Puerto Rico. Amplification values in some harbors like Puerto de Fajardo, Puerto de Naguabo and Puerto Real ranged between 2.9 and 3.8 units for frequencies between 20.7 CPD and 24.5 CPD. In the specific case of Puerto de Fajardo, a harbor's amplification value of 2.9 units was obtained from the Gaussian curve, but examining the values distribution in Figure 32 we can see a cluster between 4 and 5 units and a maximum amplification of 11. In a previous paper, Puerto de Fajardo's amplification of 5.3 units and 8.7 units were calculated for the first and second meteotsunami event, respectively; but for two other different events the values were just 5 units (Alfonso-Sosa, 2014). In addition, a maximum value of 9.6 units on August 4th 2012. All those values were calculated using a different approach, by means of the Hibiya-Kajiura Equation (1982). Summarizing, all the values obtained by means of the H-K equation ranged between 5 and 9.6 units, and the values from the amplitude distribution ranged between 1.4 and 11 units at 22 CPD. But if any value inside that range it's possible, how to select the most probable one? The answer to that question is the Gaussian fit; the Gaussian curve goes through the denser region of the amplitude distribution. Then the Gaussian curves help us to identify the most probable amplification for a particular frequency. For example the Gaussian curve shows that at a frequency of 22.9 CPD, Puerto de Fajardo's amplitude is 2.9 units. The Gaussian curves from all the harbors located at eastern Puerto Rico-connected by the same insular platform- show amplitudes smaller than 3.2 units. This result suggests that the Puerto de Fajardo's amplitudes determined by means of the H-K equation could be overestimated. In the western side of the Island, Puerto Real's Gaussian curve shows most of the amplitude values above 2 units between 14.7 CPD and 67.6 CPD, making it a harbor prone to amplification in a large range of frequencies. Puerto Real Harbor's amplifications reach a peak value at 20.7 and 50.6 CPD, these frequencies are close to the harbor response's frequencies of 18.8 CPD and 56.0 CPD determined in a previous paper (Alfonso-Sosa, 2012). Once a meteotsunami impinges on Puerto Real, we should expect two harbor seiches with similar amplitude, one with a period around 26 minutes and the second one with a period around 77 minutes. The two seiches will be excited simultaneously.

References

Alfonso-Sosa, Edwin, 2014. Meteotsunamis en el Puerto de Fajardo. Ocean Physics Education, Inc., 10 pp. https://www.academia.edu/8058659/Meteotsunamis_en_el_Puerto_de_Fajardo

Alfonso-Sosa, Edwin, 2013. The 1.8-hours Sea-Level Oscillations Recorded at Isabel Segunda, Vieques and Puerto de Fajardo. Ocean Physics Education, Inc. 22 pp. http://www.academia.edu/10073891/The_1.8-hours_Sea-Level_Oscillations_Recorded_at_Isabel_Segunda_Vieques_and_Puerto_de_Fajardo

Alfonso-Sosa, Edwin, 2012. Primer Reporte de un meteotsunami en la costa caribeña de Puerto Rico. Ocean Physics Education, Inc., 24 pp. https://www.academia.edu/4951196/Primer_Reporte_de_un_Meteotsunami_en_la_Costa_Caribena_de_Puerto_Rico

Allen, S. C. R. and D. J. M. Greenslade. 2009. A Spectral Climatology of Australian and South-West Pacific Tide Gauges, CAWCR Technical Report No. 011. CSIRO. Bureau of Meteorolgy, Australian Government.

Hibiya T. and K. Kajiura, 1982. Origin of the Abiki Phenomenon (a kind of seiche) in Nagasaki Bay. Journal of the Oceanographic Society of Japan, Vol. 38, pp. 172-182.

Huang, N. E., Shih, H. H., Shen, Z., Long, S. R., and K. L. Fan. 2000. The ages of large amplitude coastal seiches on the Caribbean Coast of Puerto Rico. Journal of Physical Oceanography 30(8), 2001-2012.

Huang, N. E., Shen, Z., and S. R. Long, M. C. Wu, H. H. Shih, Q. Zheng, N-C. Yen, C. C. Tung, and H. H. Liu. 1998. The empirical mode decomposition and the Hilbert spectrum fon nonlinear and non-stationary time series analysis, Proc. R. Soc. London Series A 454: 903-995.

Huang, N. E., Shen Z. and S. R. Long. 1999. A new view of nonlinear water waves: the Hilbert Spectrum, Annual Review of Fluid Dynamics 31:417-457.

Figures

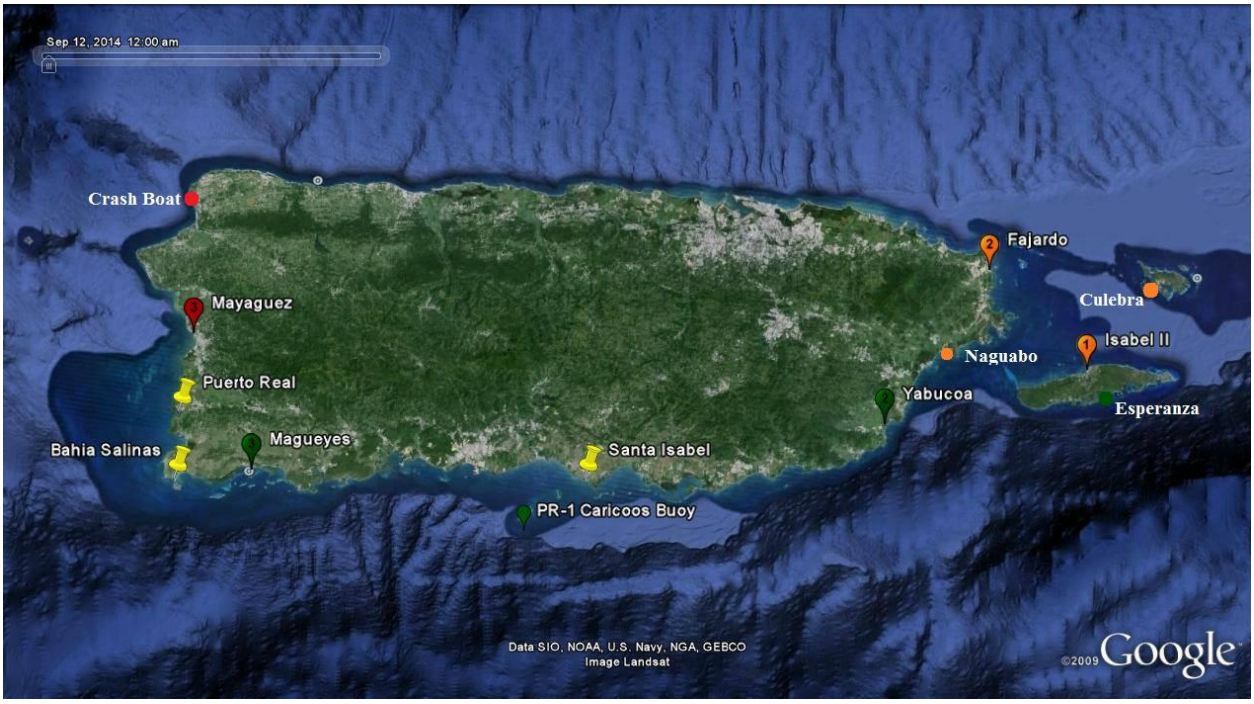

Figure 1

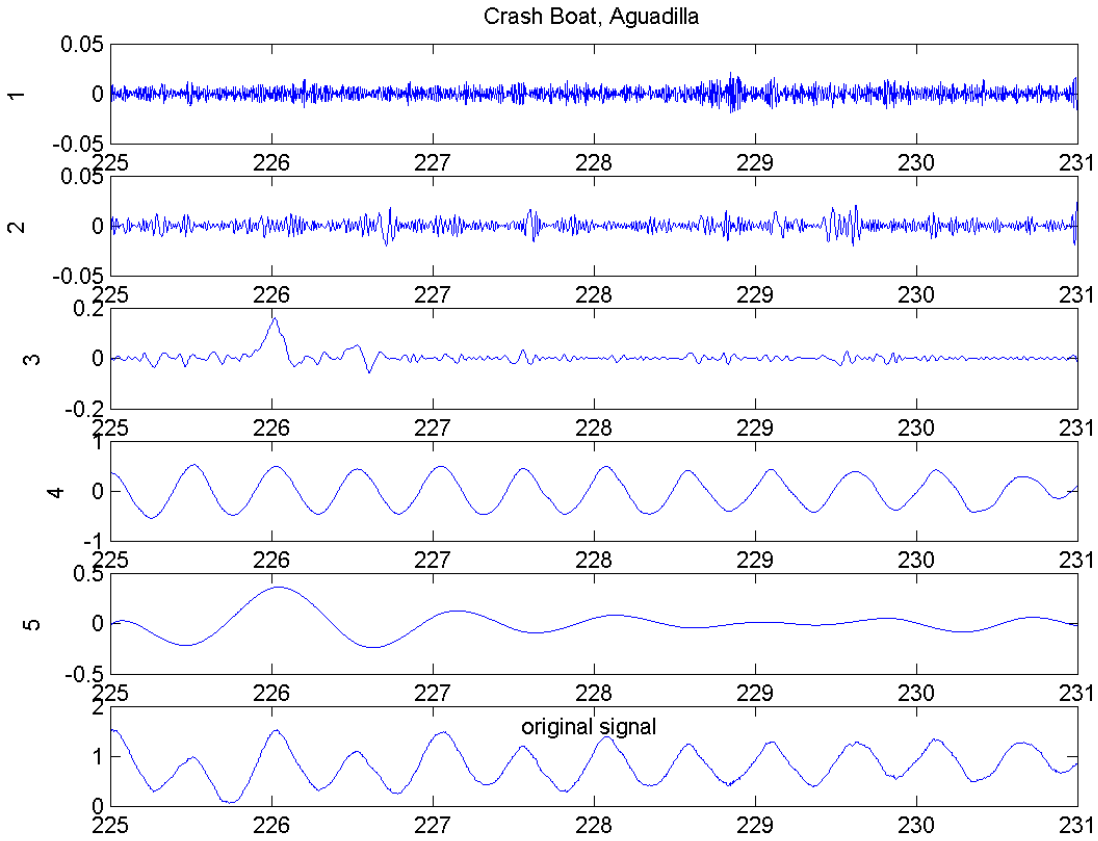
Crash Boat, Aguadilla
0.05
0
-0.05
1
225
226
227
228
229
230
231
0.05
0
-0.05
2
0.2
0
-0.2
3
1
0
-1
4
0.5
0
-0.5
5
2
1
0
original signal

Figure 2

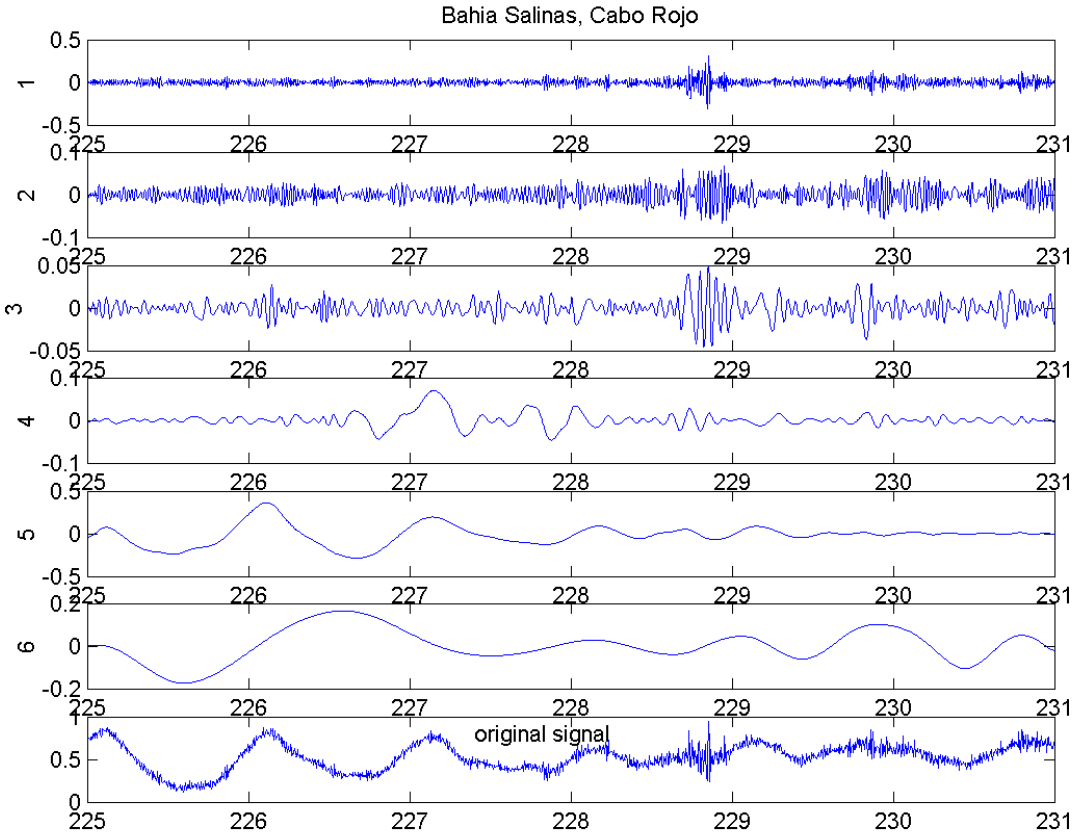
Bahia Salinas, Cabo Rojo
1
2
3
4
5
6
original signal
225
226
227
228
229
230
231

Figure 3

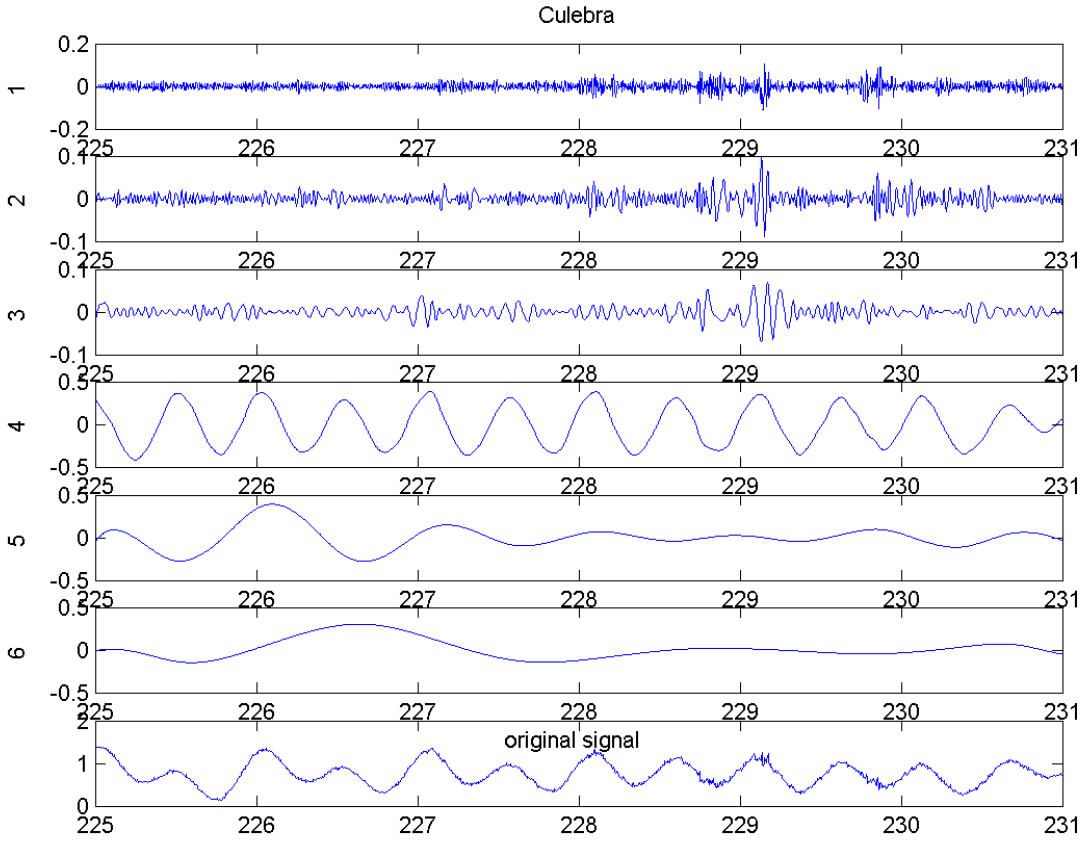

Figure 4

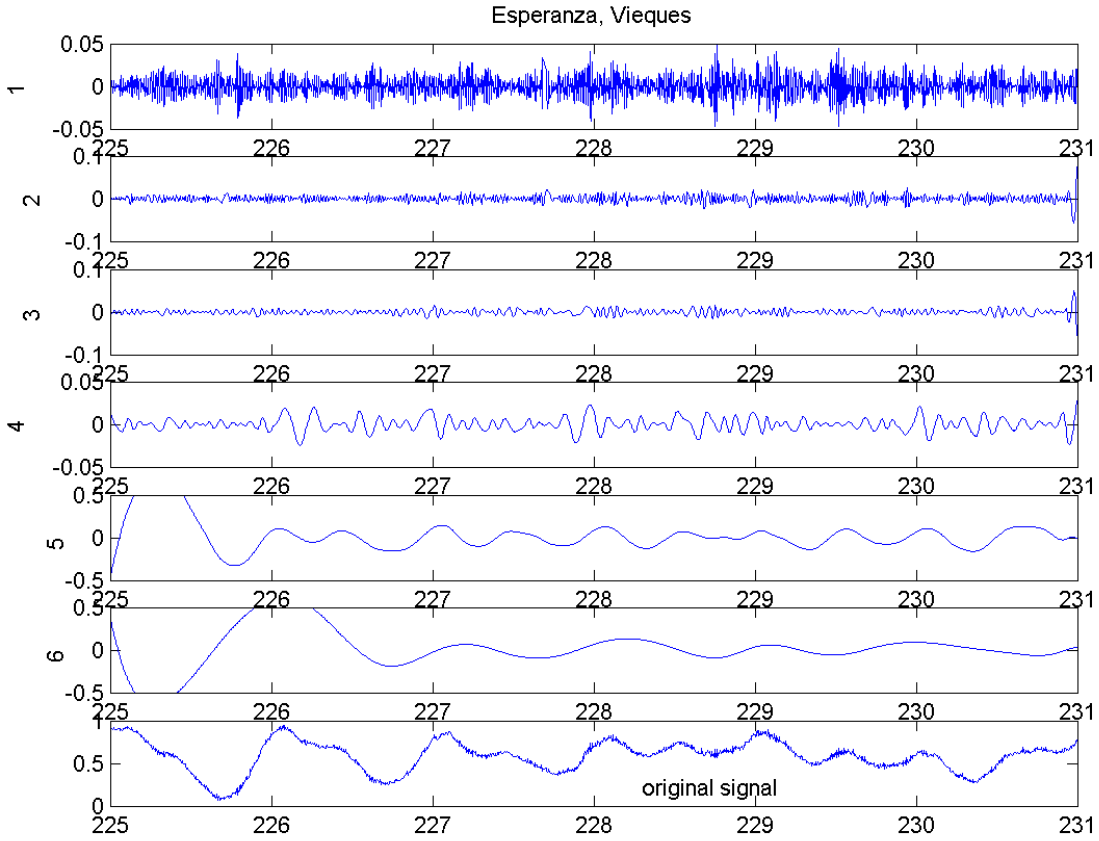
Esperanza, Vieques
1
2
3
4
5
6
original signal
225
226
227
228
229
230
231

Figure 5

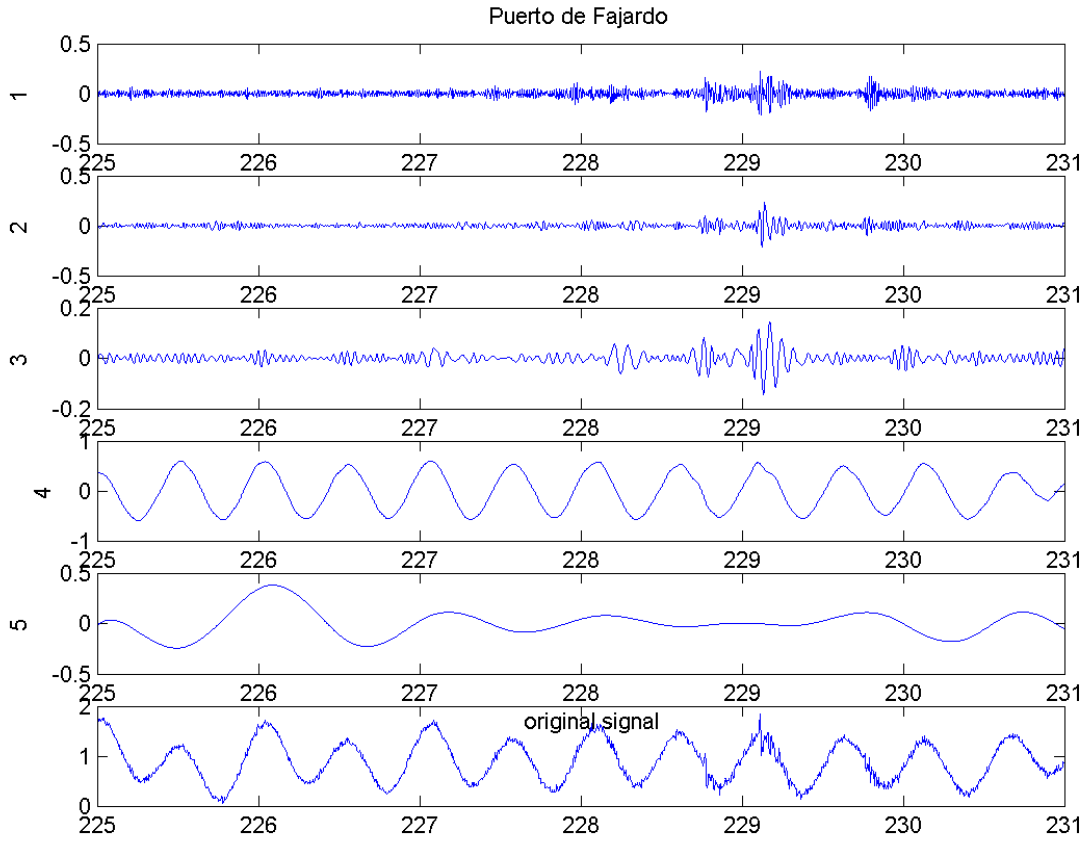
Puerto de Fajardo
1
2
3
4
5
original signal
225
226
227
228
229
230
231

Figure 6

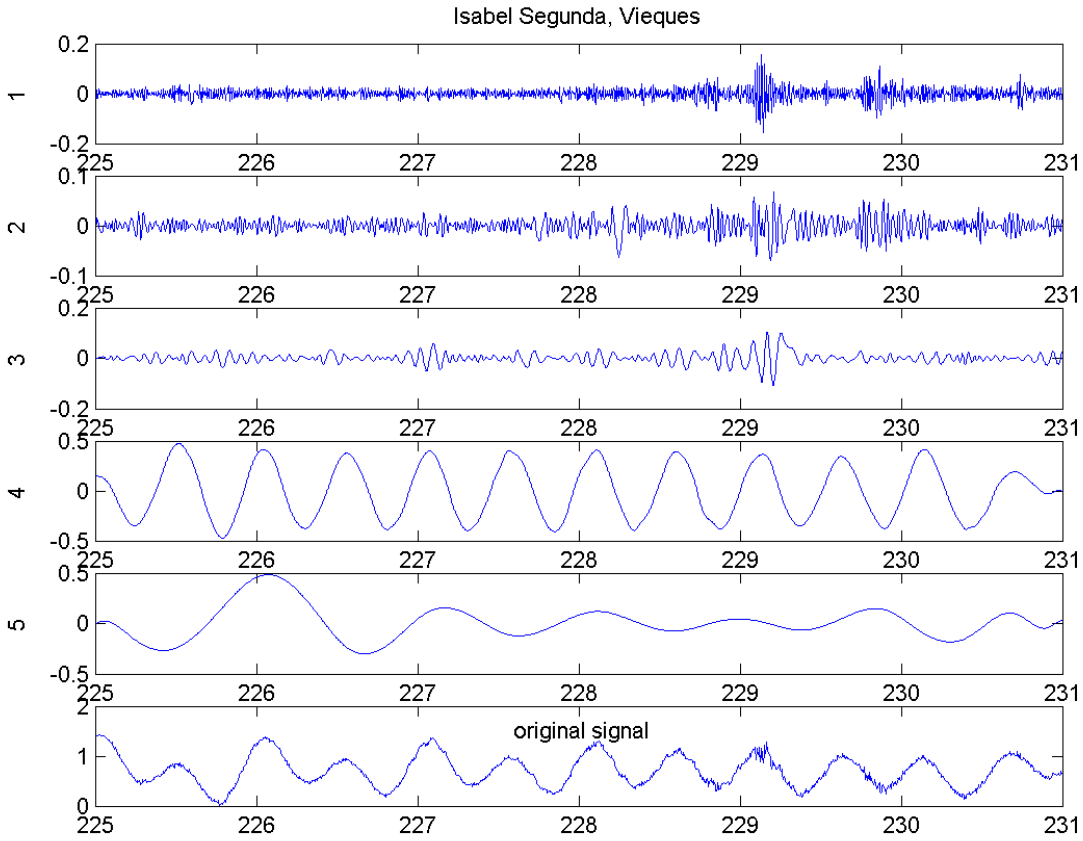

Figure 7

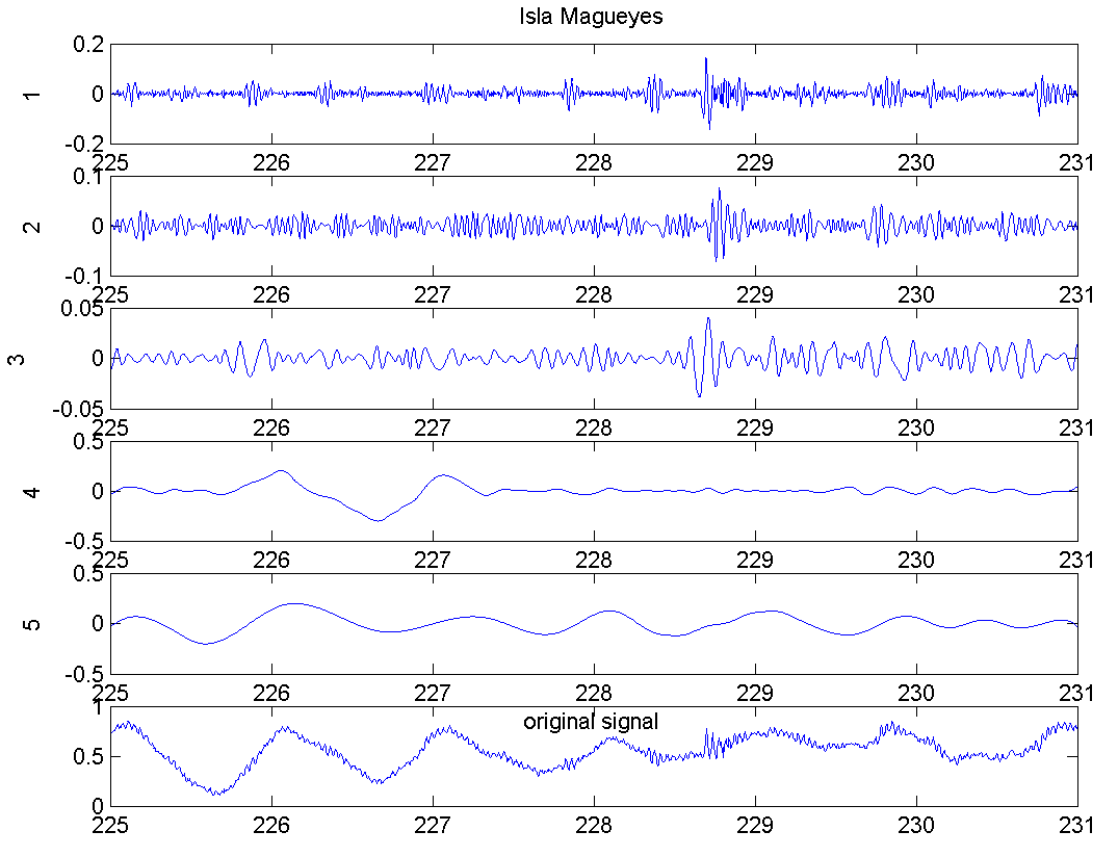
Isla Magueyes
1
2
3
4
5
original signal
225
226
227
228
229
230
231

Figure 8

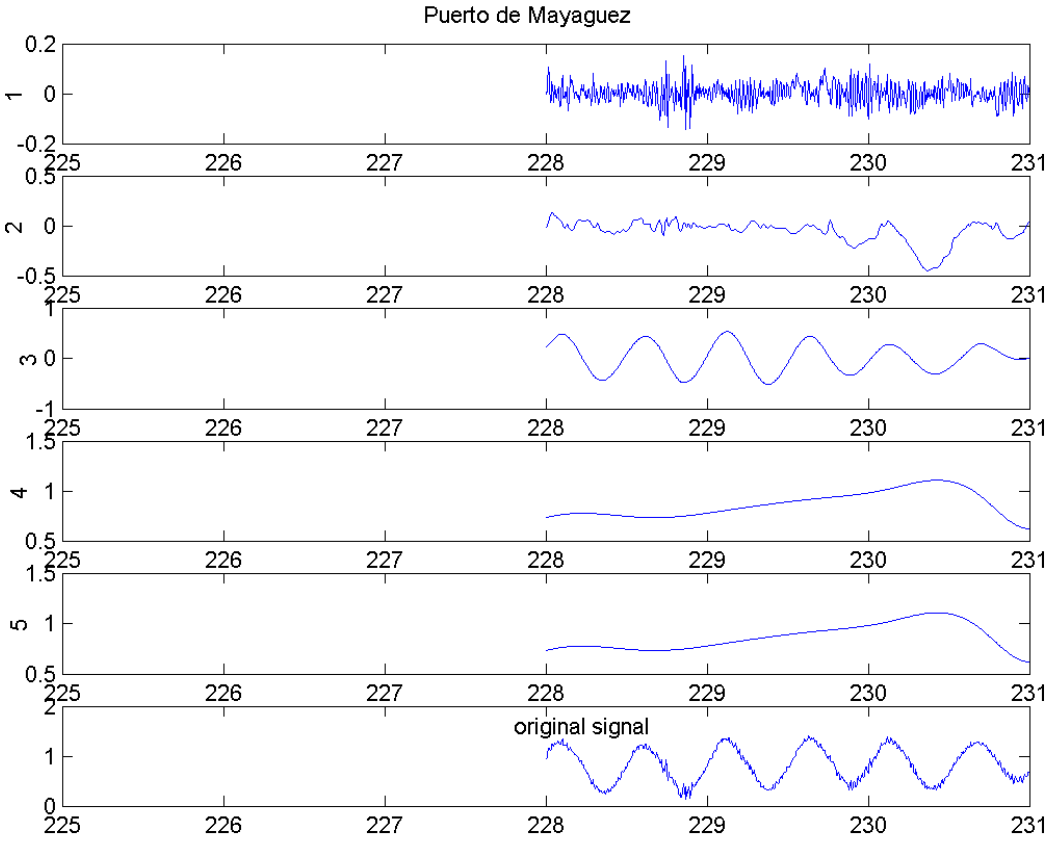
Puerto de Mayaguez
1
2
3
4
5
original signal
225
226
227
228
229
230
231

Figure 9

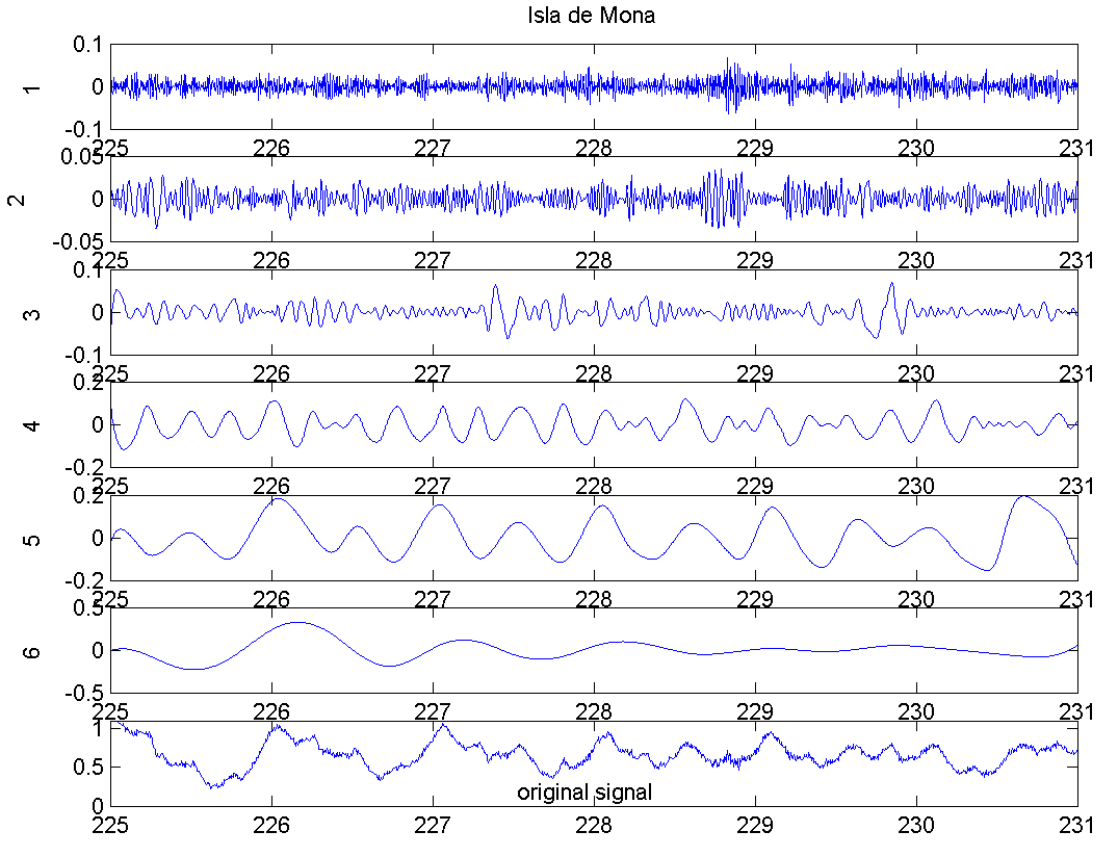
Isla de Mona
1
2
3
4
5
6
original signal
225
226
227
228
229
230
231

Figure 10

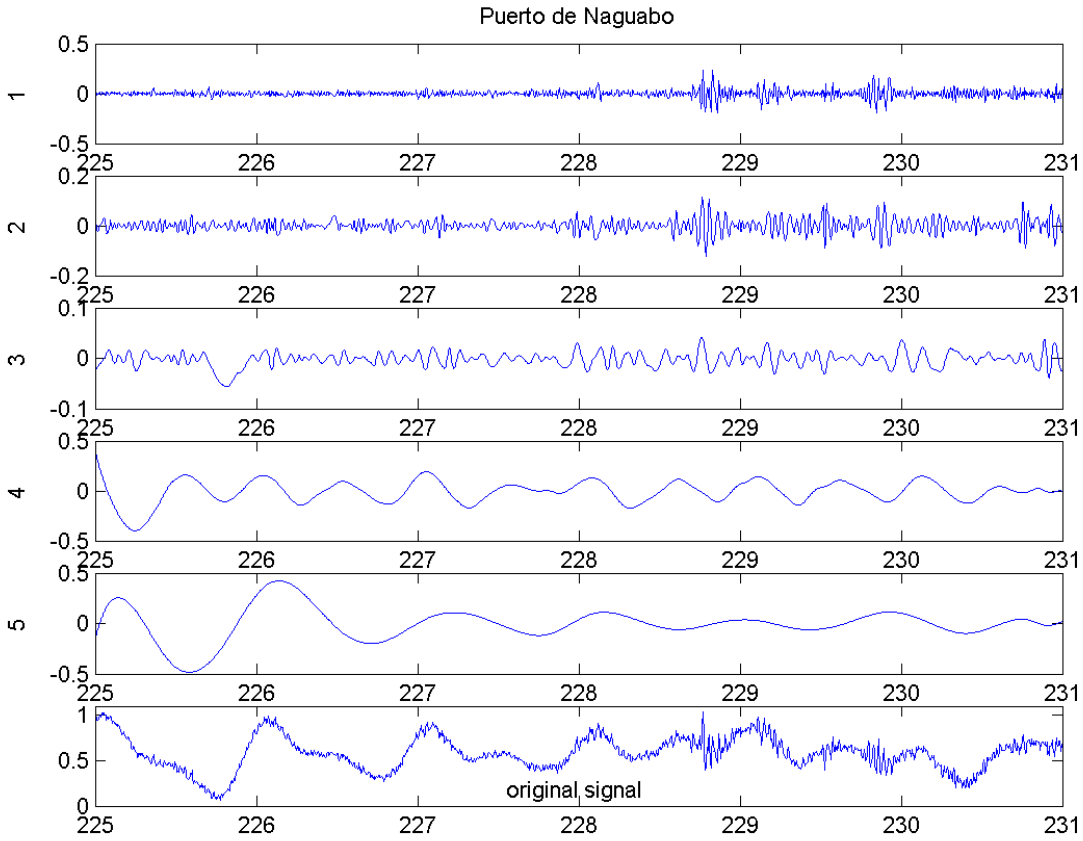
Puerto de Naguabo
1
2
3
4
5
original signal
225
226
227
228
229
230
231

Figure 11

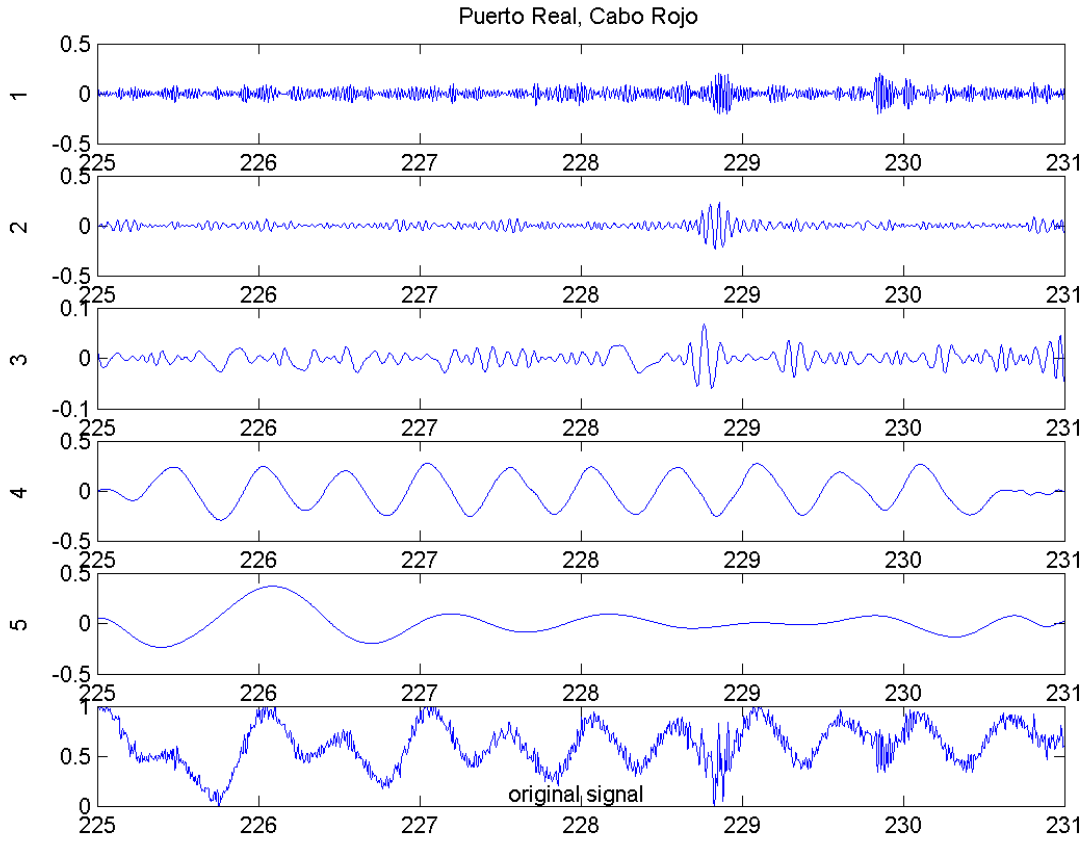
Puerto Real, Cabo Rojo
1
2
3
4
5
0.5
0
-0.5
0.1
-0.1
1
225
226
227
228
229
230
231
original signal

Figure 12

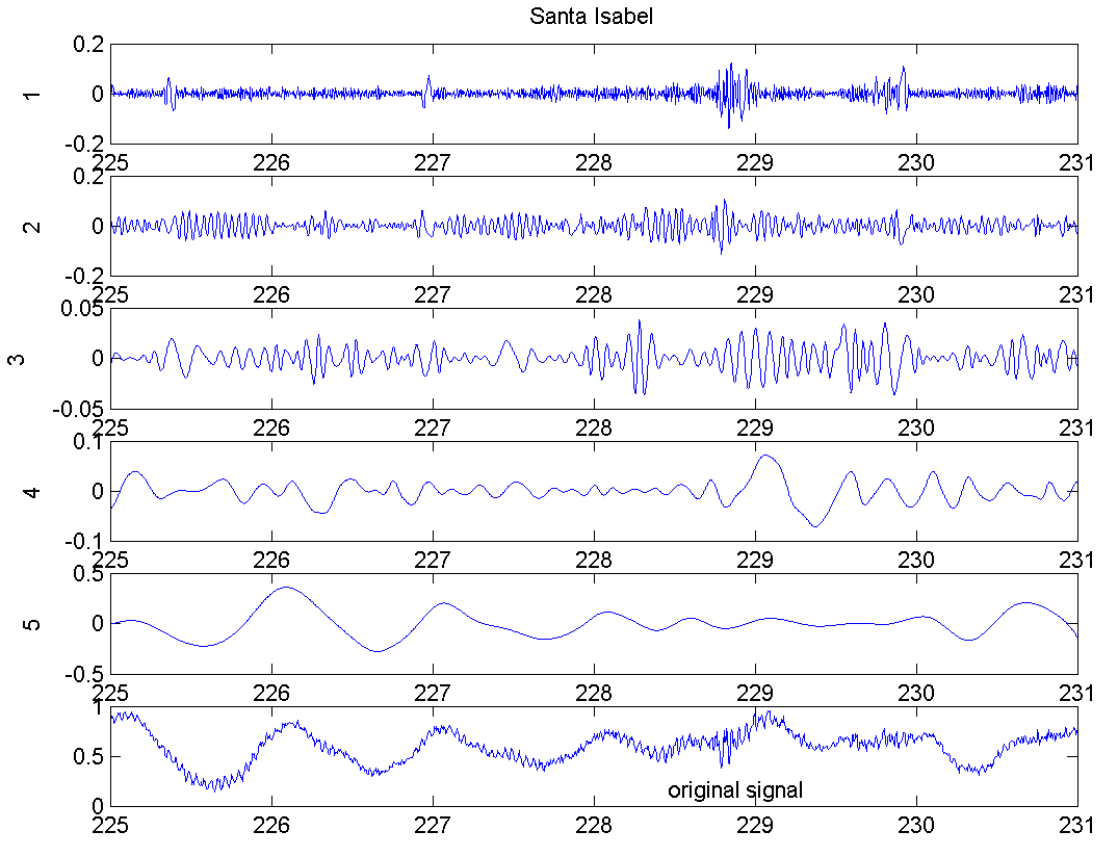
Santa Isabel
1
2
3
4
5
original signal
225
226
227
228
229
230
231

Figure 13

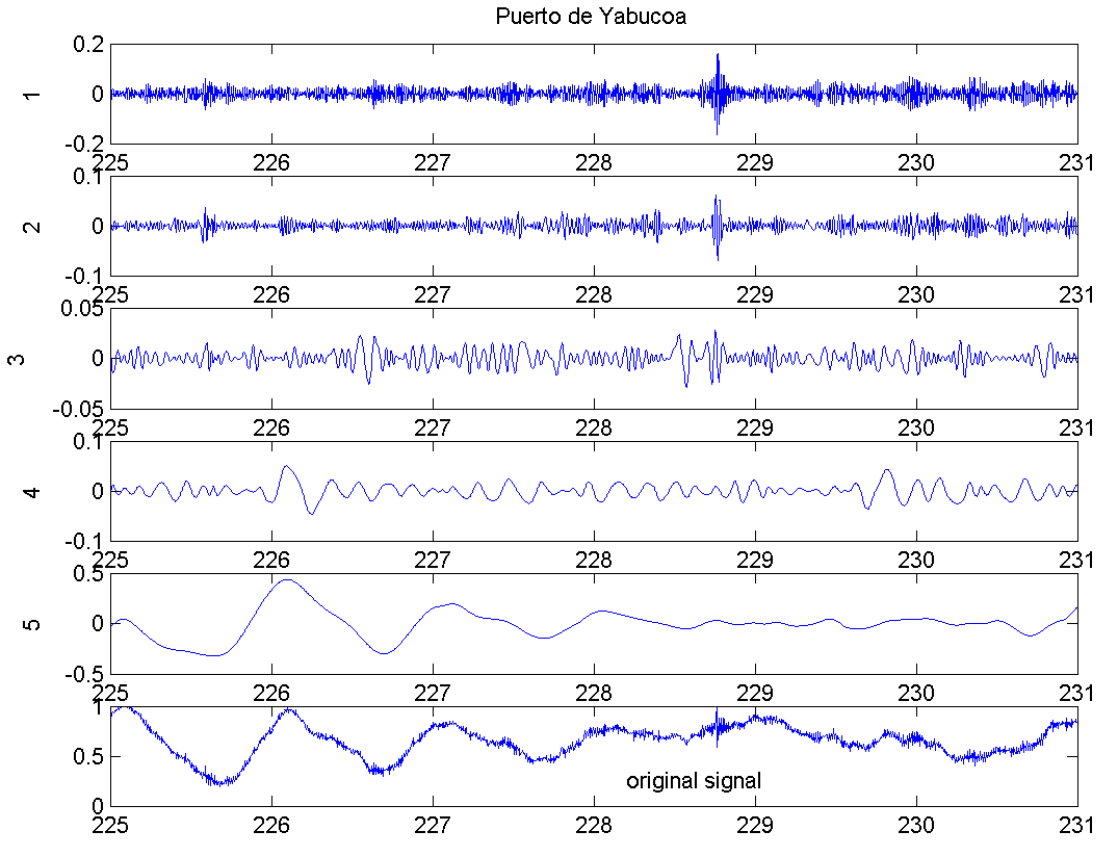
Puerto de Yabucoa
1
2
3
4
5
original signal
225
226
227
228
229
230
231

Figure 14

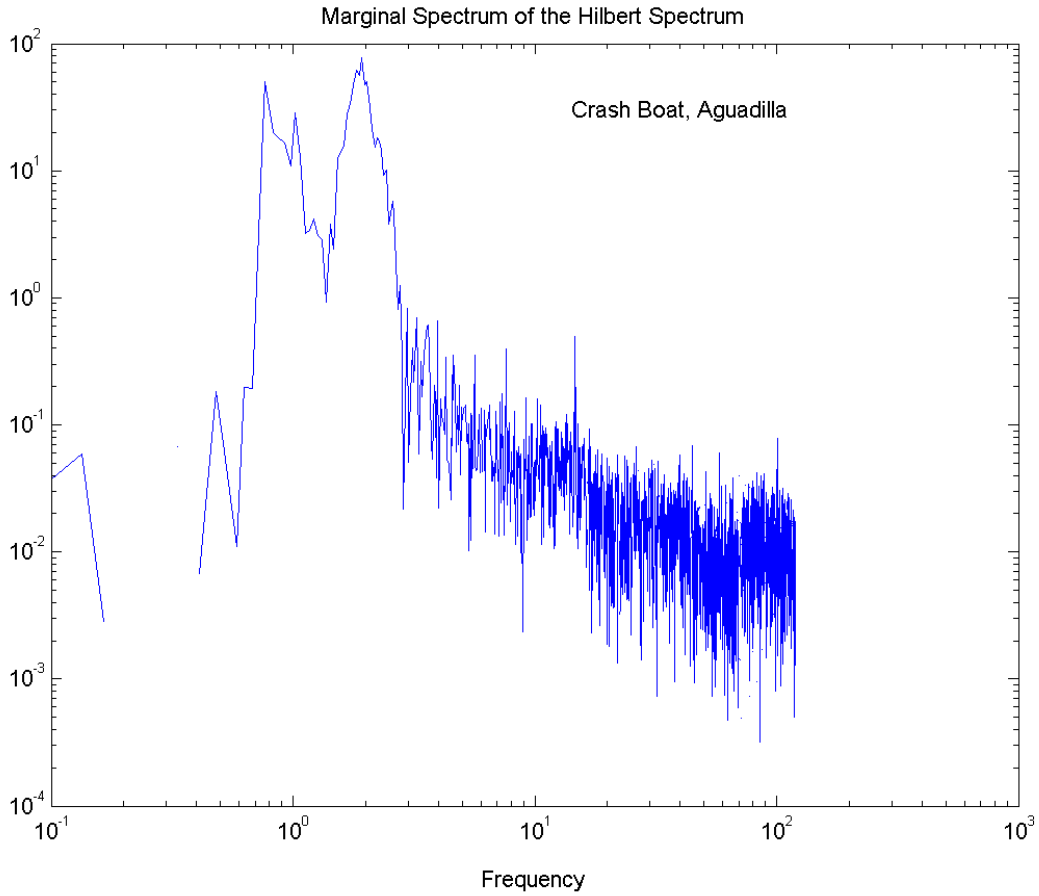
Marginal Spectrum of the Hilbert Spectrum
Crash Boat, Aguadilla
Frequency

Figure 15

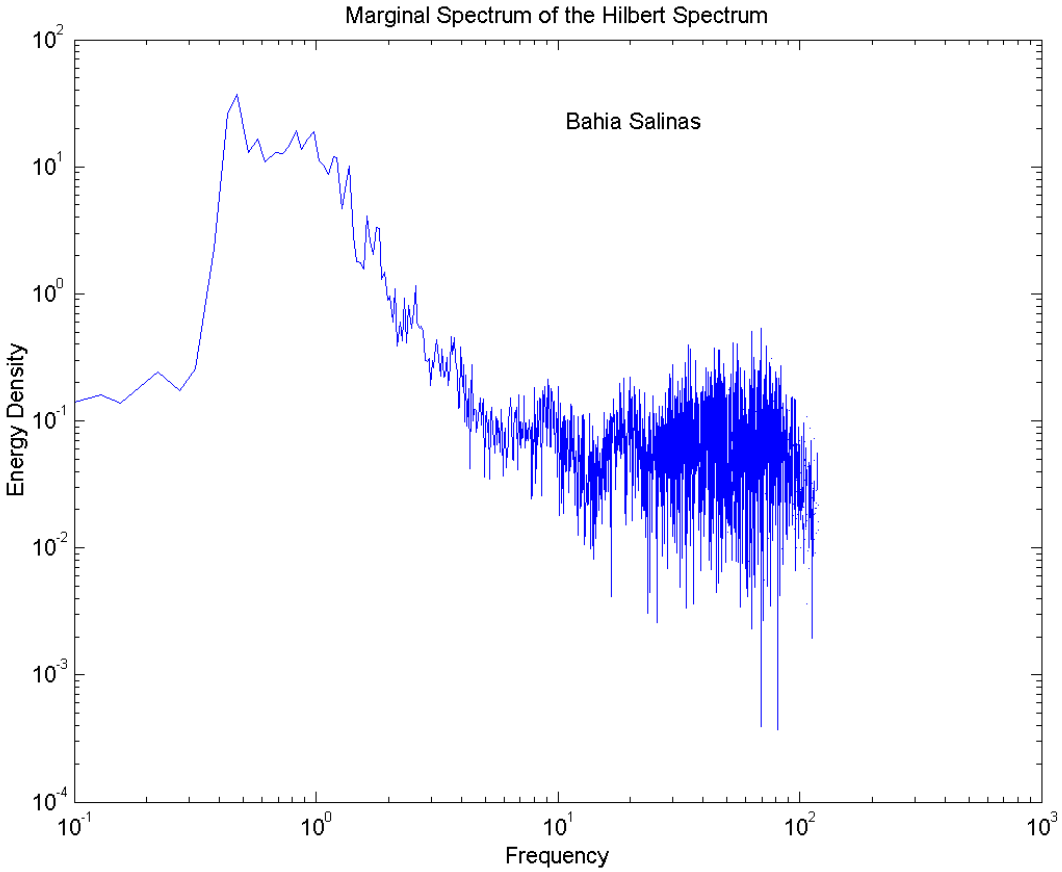
Marginal Spectrum of the Hilbert Spectrum
Bahia Salinas
Energy Density
Frequency
10^{2}
10^{1}
10^{0}
10^{-1}
10^{-2}
10^{-3}
10^{-4}
10^{-1}
10^{0}
10^{1}
10^{2}
10^{3}

Figure 16

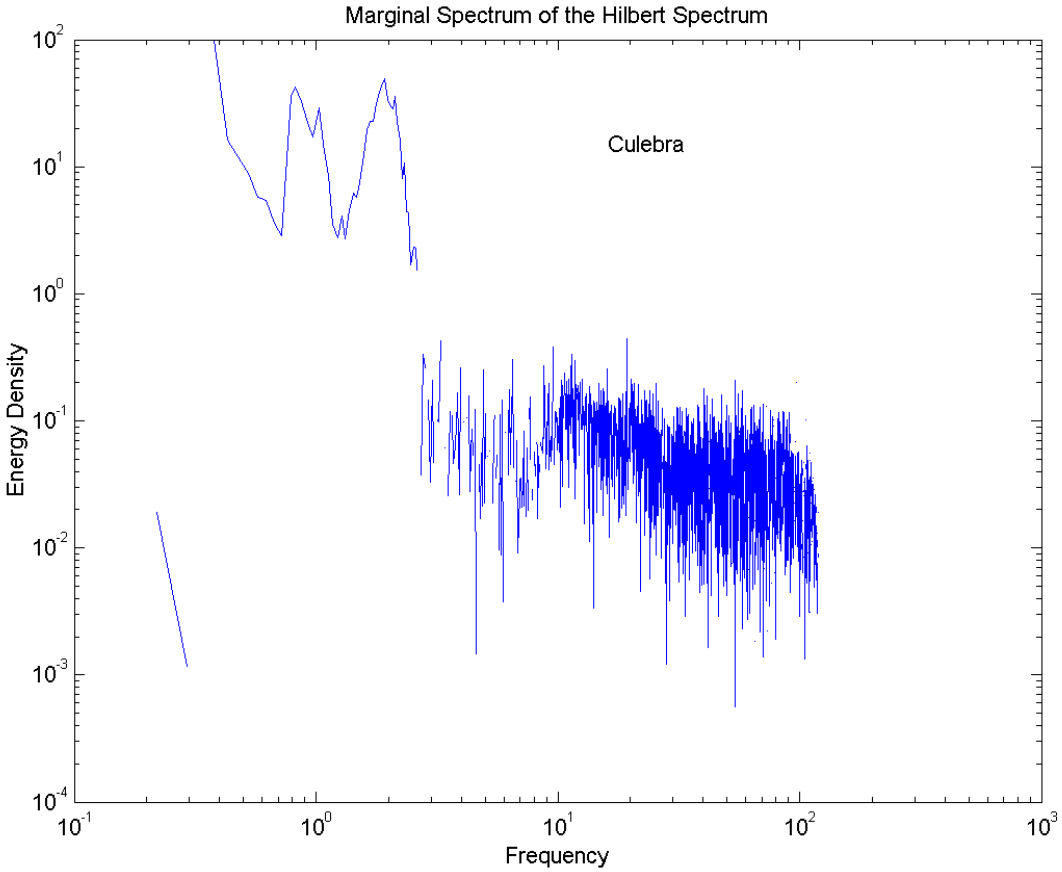
Marginal Spectrum of the Hilbert Spectrum
Culebra
Energy Density
Frequency
10^{2}
10^{1}
10^{0}
10^{-1}
10^{-2}
10^{-3}
10^{-4}
10^{-1}
10^{0}
10^{1}
10^{2}
10^{3}

Figure 17

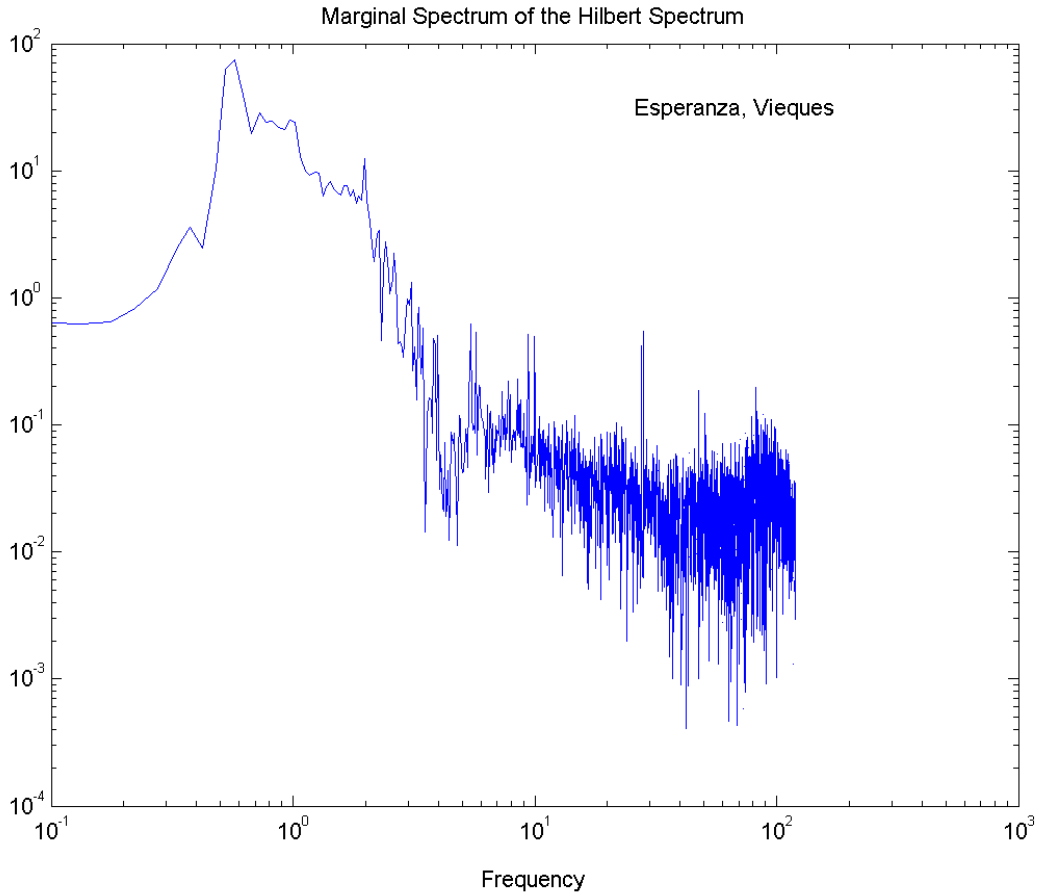
Marginal Spectrum of the Hilbert Spectrum
Esperanza, Vieques
Frequency

Figure 18

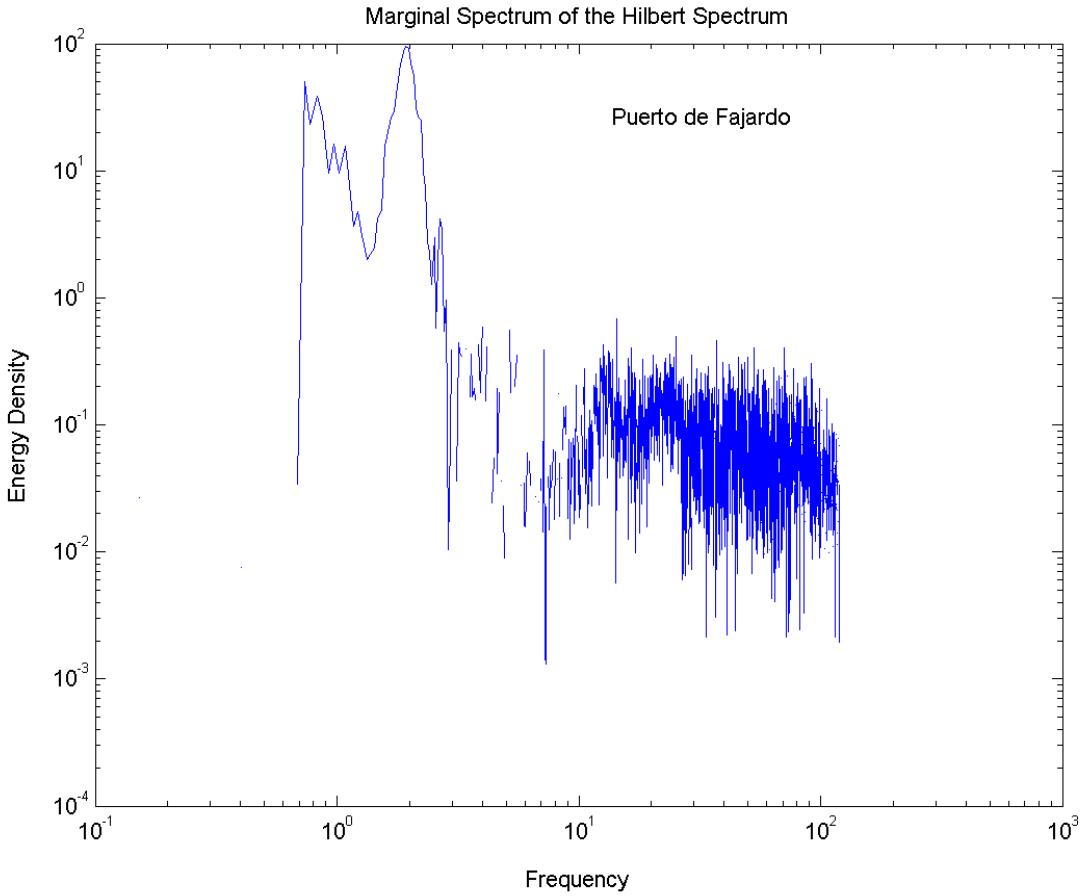
Marginal Spectrum of the Hilbert Spectrum
Puerto de Fajardo
Energy Density
Frequency
10^{2}
10^{1}
10^{0}
10^{-1}
10^{-2}
10^{-3}
10^{-4}
10^{-1}
10^{0}
10^{1}
10^{2}
10^{3}

Figure 19

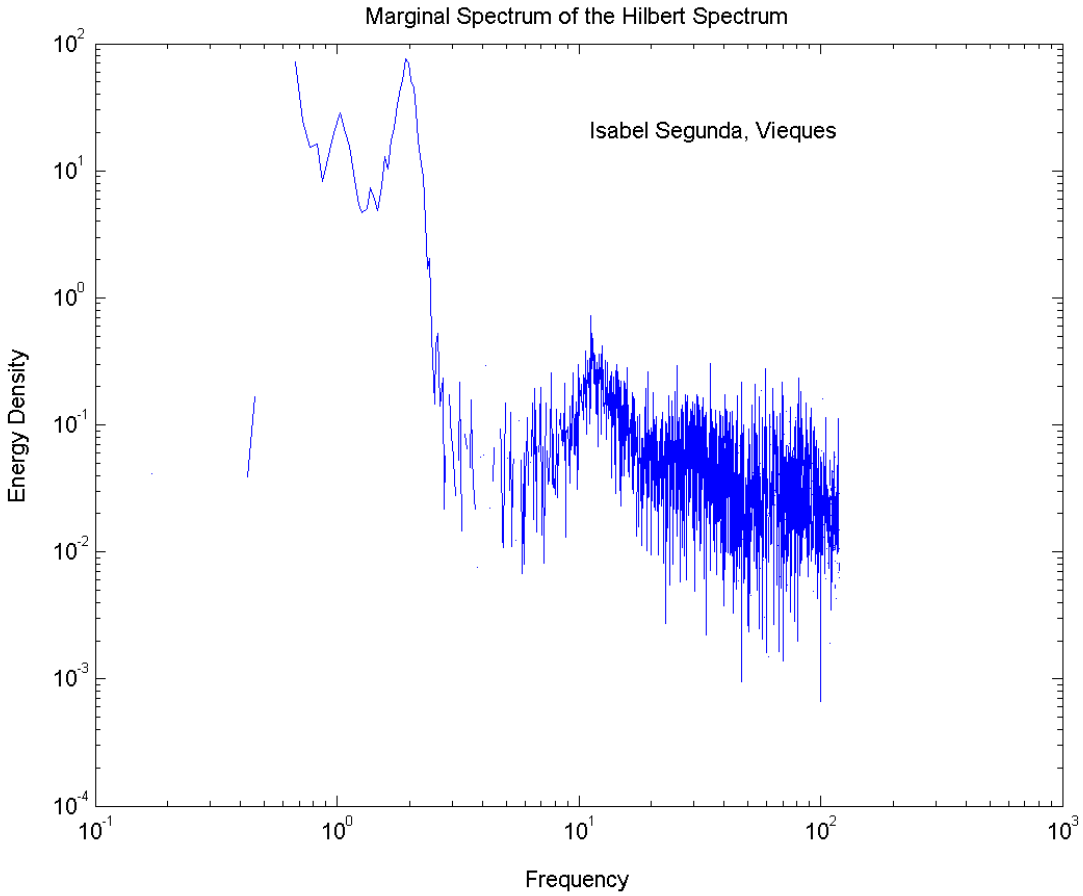
Marginal Spectrum of the Hilbert Spectrum
Isabel Segunda, Vieques
Energy Density
Frequency
10^{2}
10^{1}
10^{0}
10^{-1}
10^{-2}
10^{-3}
10^{-4}
10^{-1}
10^{0}
10^{1}
10^{2}
10^{3}

Figure 20

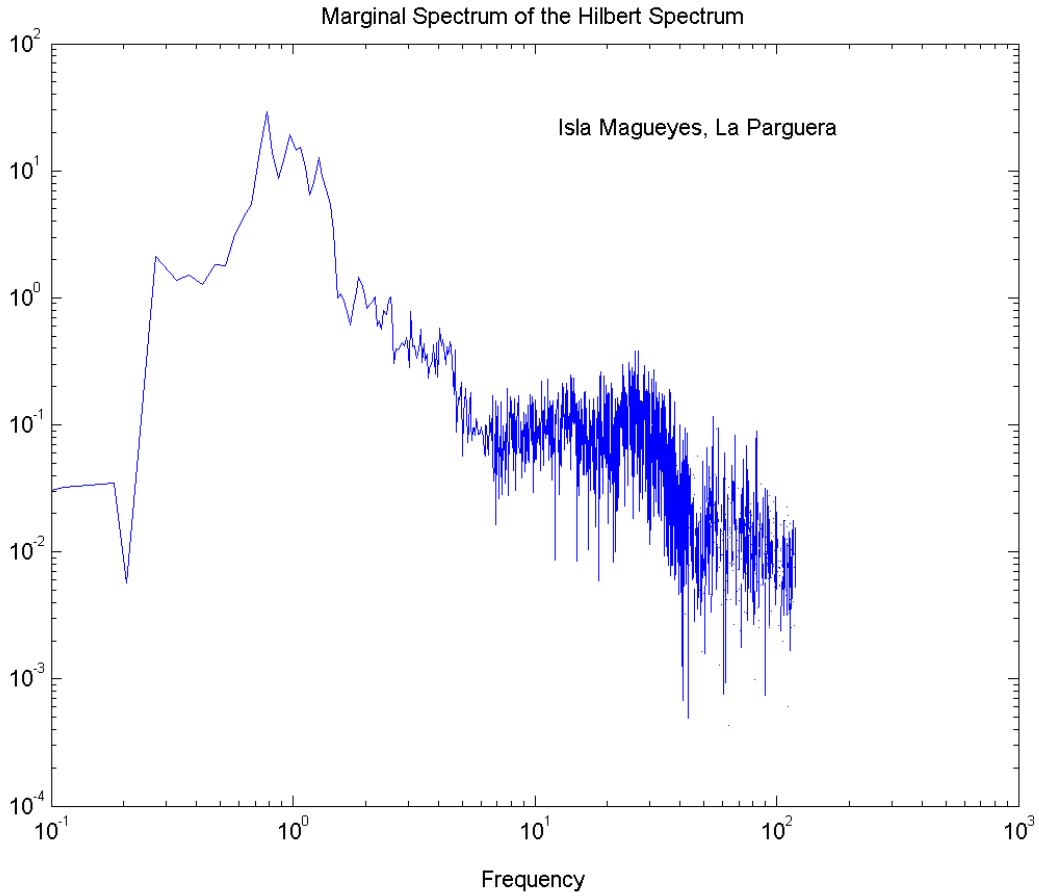
Marginal Spectrum of the Hilbert Spectrum
Isla Magueyes, La Parguera
Frequency

Figure 21

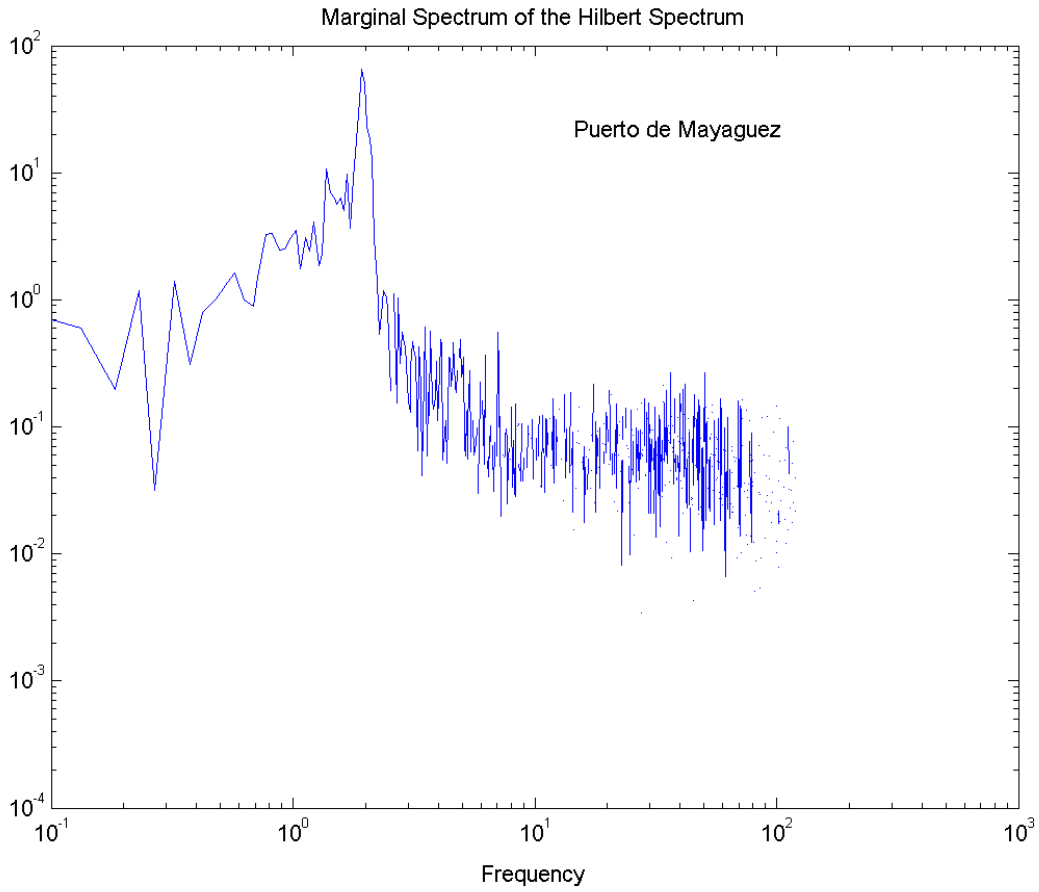
Marginal Spectrum of the Hilbert Spectrum
Puerto de Mayaguez
Frequency

Figure 22

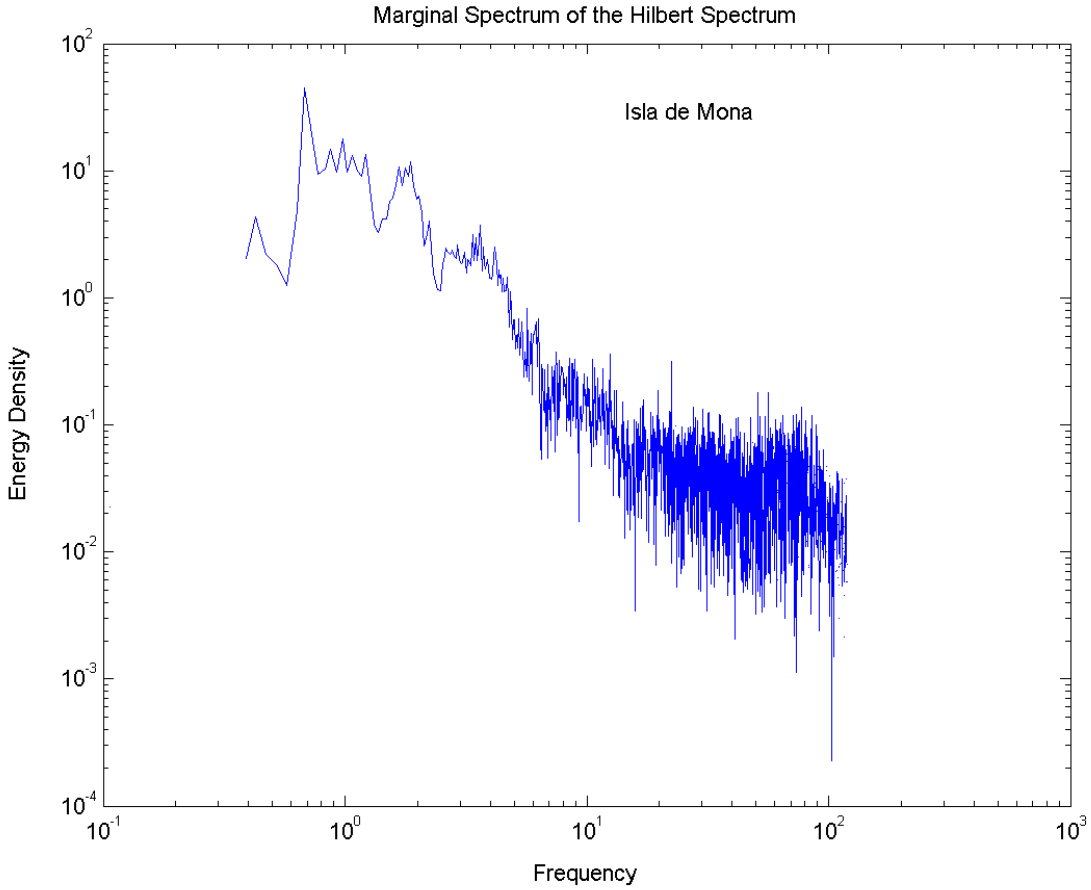
Marginal Spectrum of the Hilbert Spectrum
Isla de Mona
Energy Density
Frequency
10^{2}
10^{1}
10^{0}
10^{-1}
10^{-2}
10^{-3}
10^{-4}
10^{-1}
10^{0}
10^{1}
10^{2}
10^{3}

Figure 23

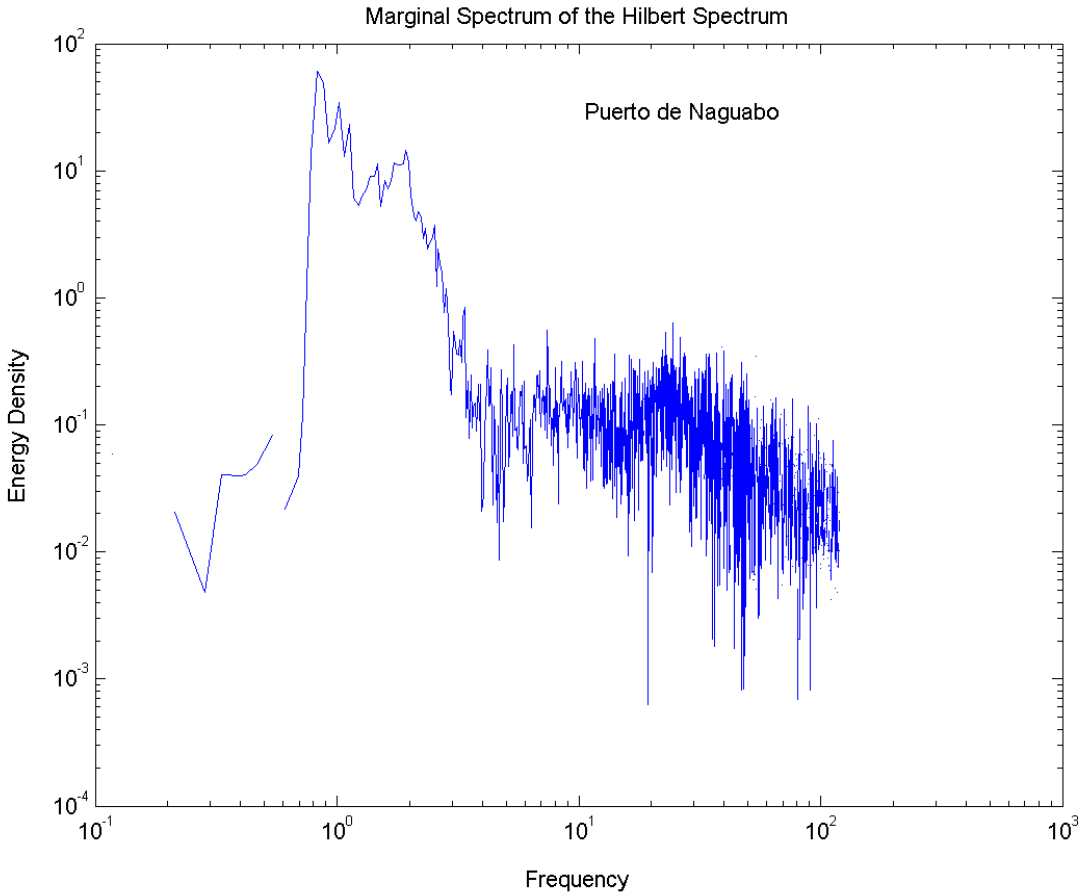
Marginal Spectrum of the Hilbert Spectrum
Puerto de Naguabo
Energy Density
Frequency
10^{2}
10^{1}
10^{0}
10^{-1}
10^{-2}
10^{-3}
10^{-4}
10^{-1}
10^{0}
10^{1}
10^{2}
10^{3}

Figure 24

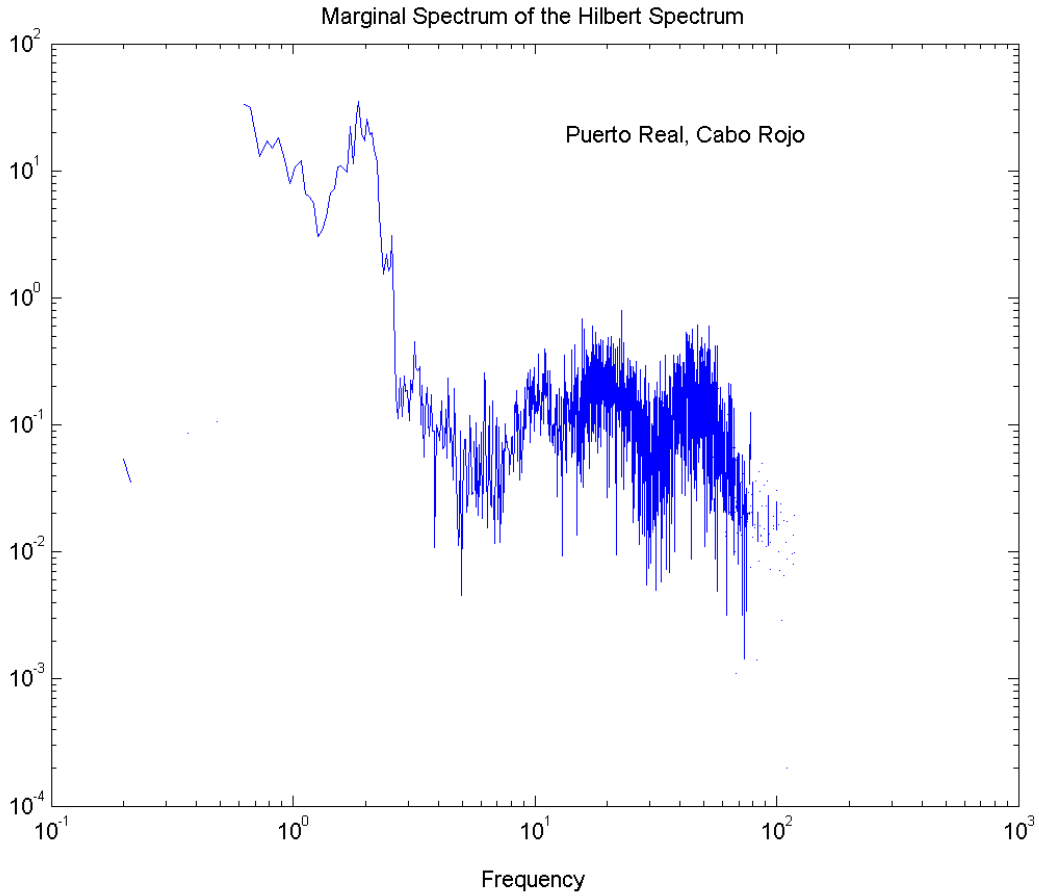
Marginal Spectrum of the Hilbert Spectrum
Puerto Real, Cabo Rojo
Frequency

Figure 25

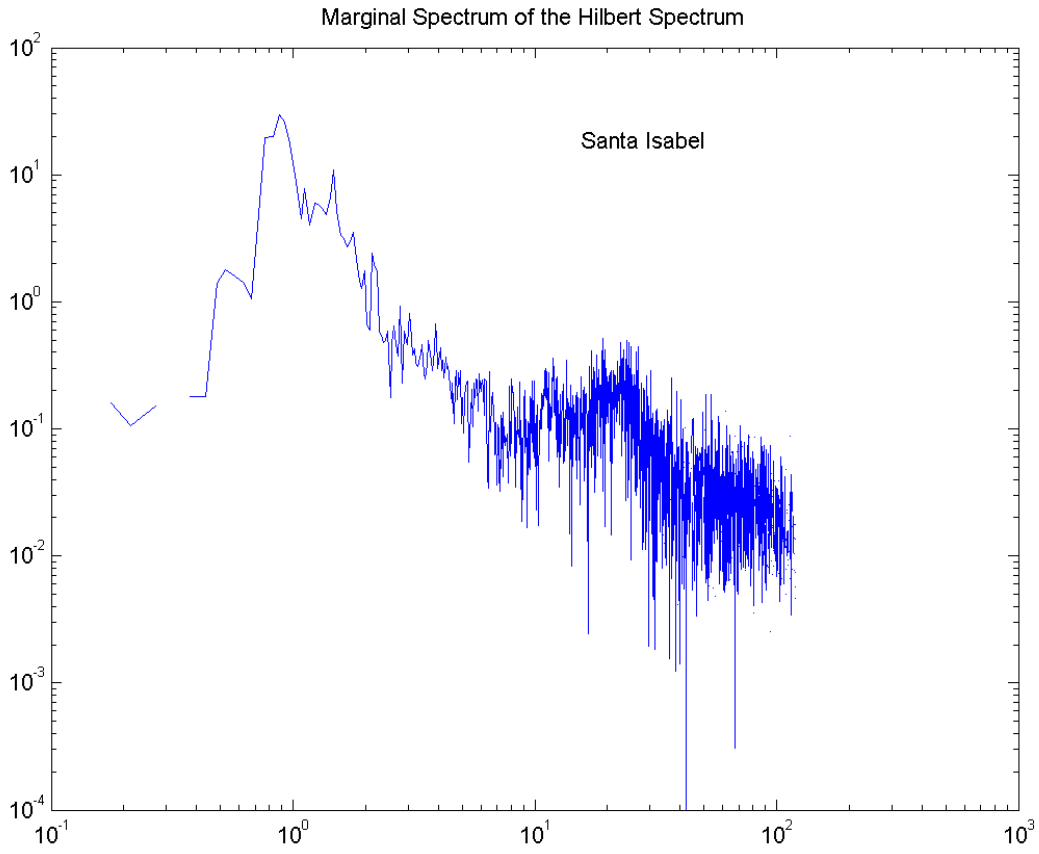
Marginal Spectrum of the Hilbert Spectrum
Santa Isabel
10^{2}
10^{1}
10^{0}
10^{-1}
10^{-2}
10^{-3}
10^{-4}
10^{-1}
10^{0}
10^{1}
10^{2}
10^{3}

Figure 26

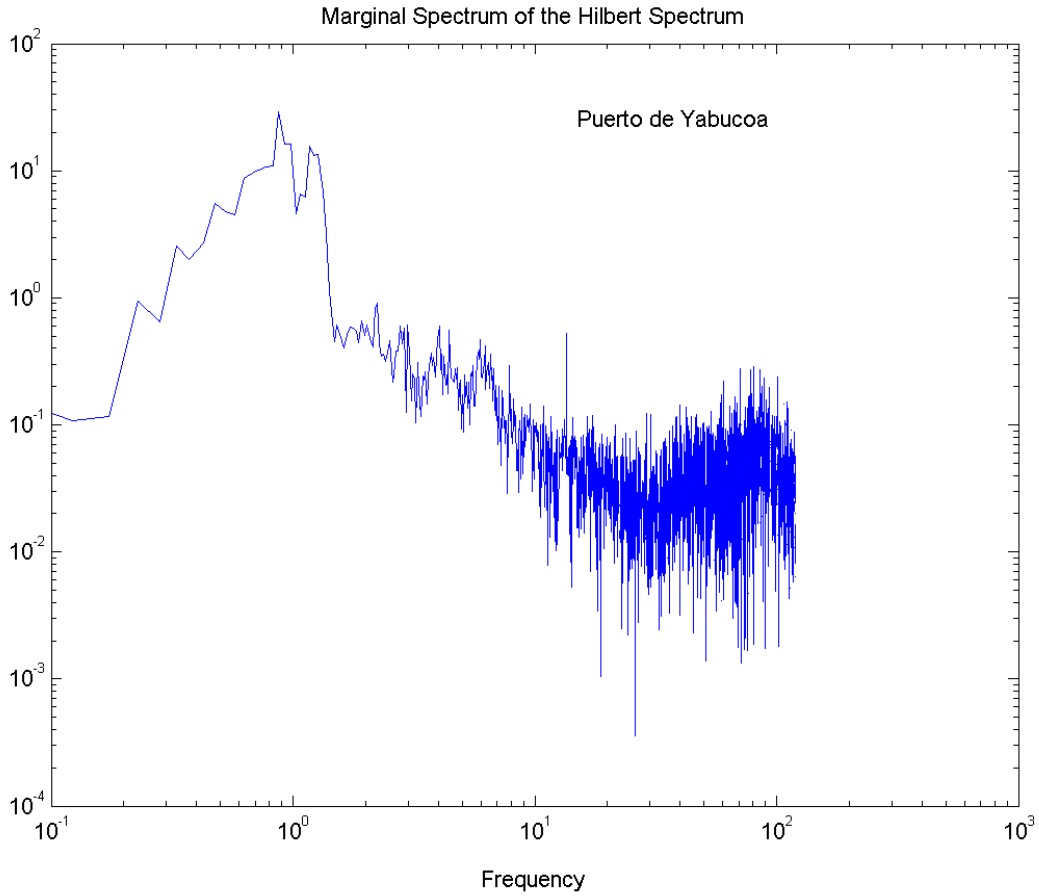
Marginal Spectrum of the Hilbert Spectrum
Puerto de Yabucoa
Frequency

Figure 27

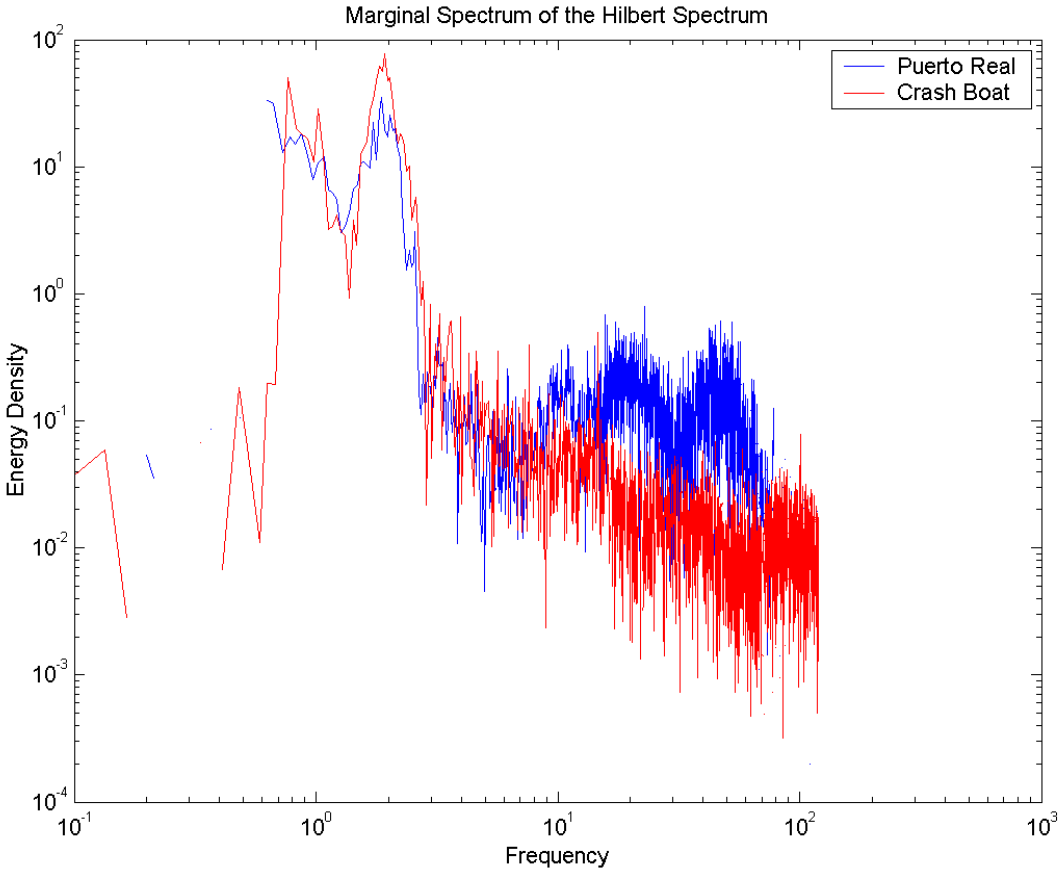
Marginal Spectrum of the Hilbert Spectrum
Puerto Real
Crash Boat
Energy Density
Frequency
10^{2}
10^{1}
10^{0}
10^{-1}
10^{-2}
10^{-3}
10^{-4}
10^{-1}
10^{0}
10^{1}
10^{2}
10^{3}

Figure 28

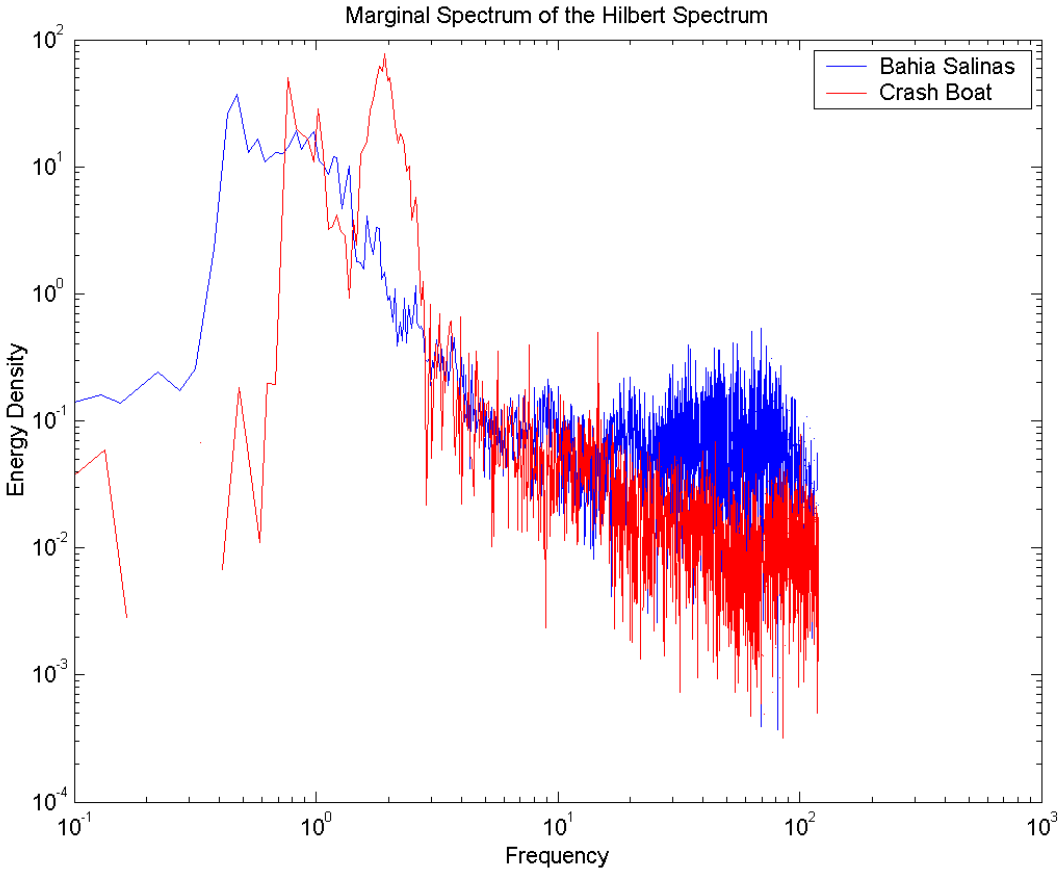
Marginal Spectrum of the Hilbert Spectrum
Bahia Salinas
Crash Boat
Energy Density
Frequency
10^{2}
10^{1}
10^{0}
10^{-1}
10^{-2}
10^{-3}
10^{-4}
10^{-1}
10^{0}
10^{1}
10^{2}
10^{3}

Figure 29

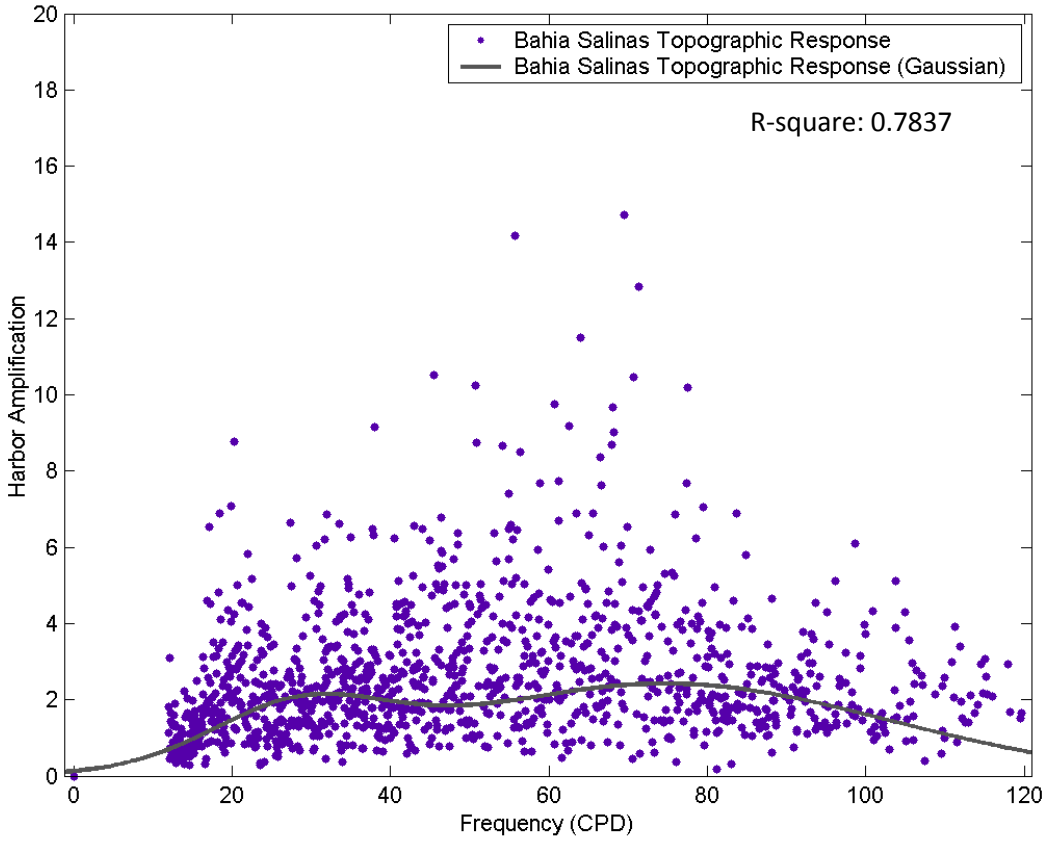
Bahia Salinas Topographic Response
Bahia Salinas Topographic Response (Gaussian)
R-square: 0.7837
Harbor Amplification
Frequency (CPD)
0
2
4
6
8
10
12
14
16
18
20
0
20
40
60
80
100
120

Figure 30

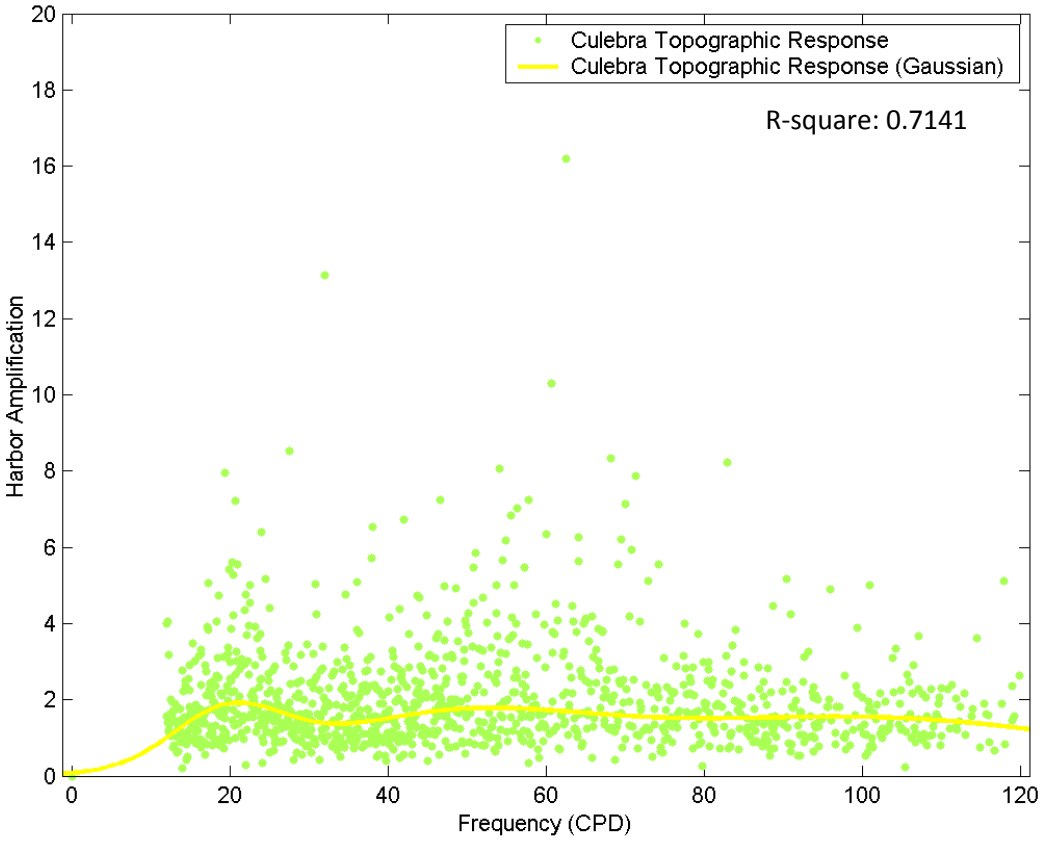
Culebra Topographic Response
Culebra Topographic Response (Gaussian)
R-square: 0.7141
Harbor Amplification
Frequency (CPD)
0
2
4
6
8
10
12
14
16
18
20
0
20
40
60
80
100
120

Figurre 31

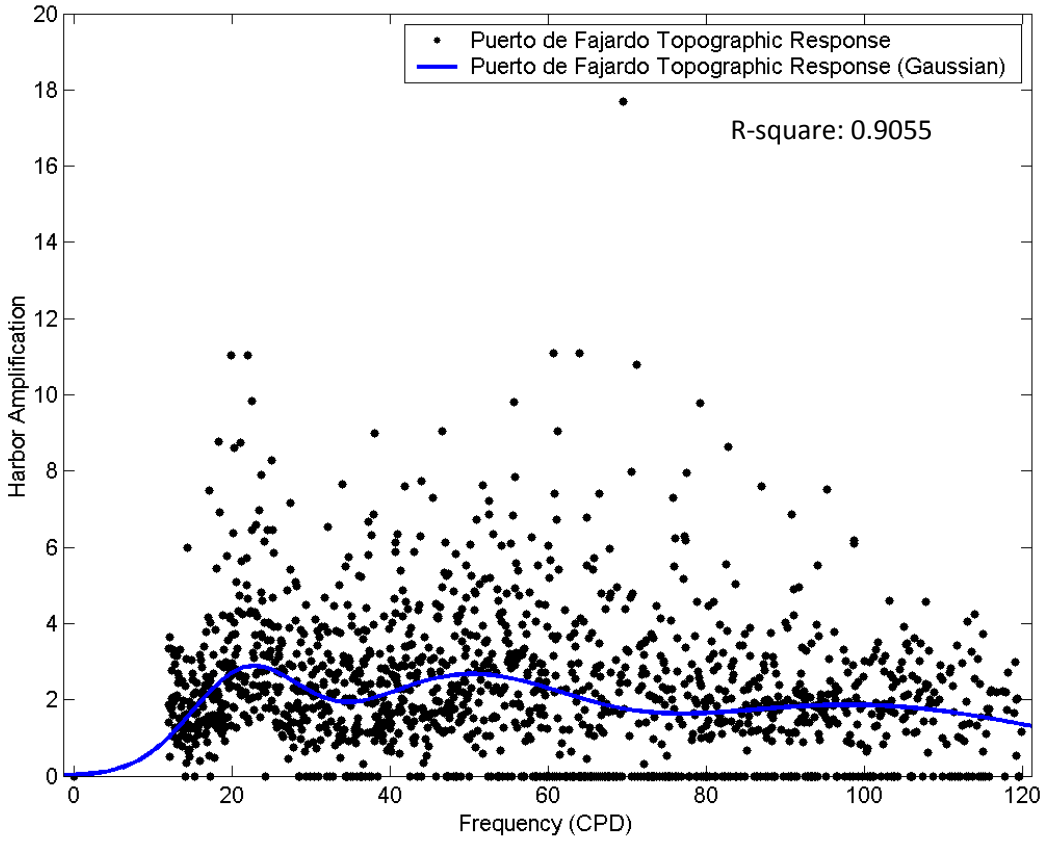
Puerto de Fajardo Topographic Response
Puerto de Fajardo Topographic Response (Gaussian)
R-square: 0.9055
Harbor Amplification
Frequency (CPD)
0
2
4
6
8
10
12
14
16
18
20
0
20
40
60
80
100
120

Figure 32

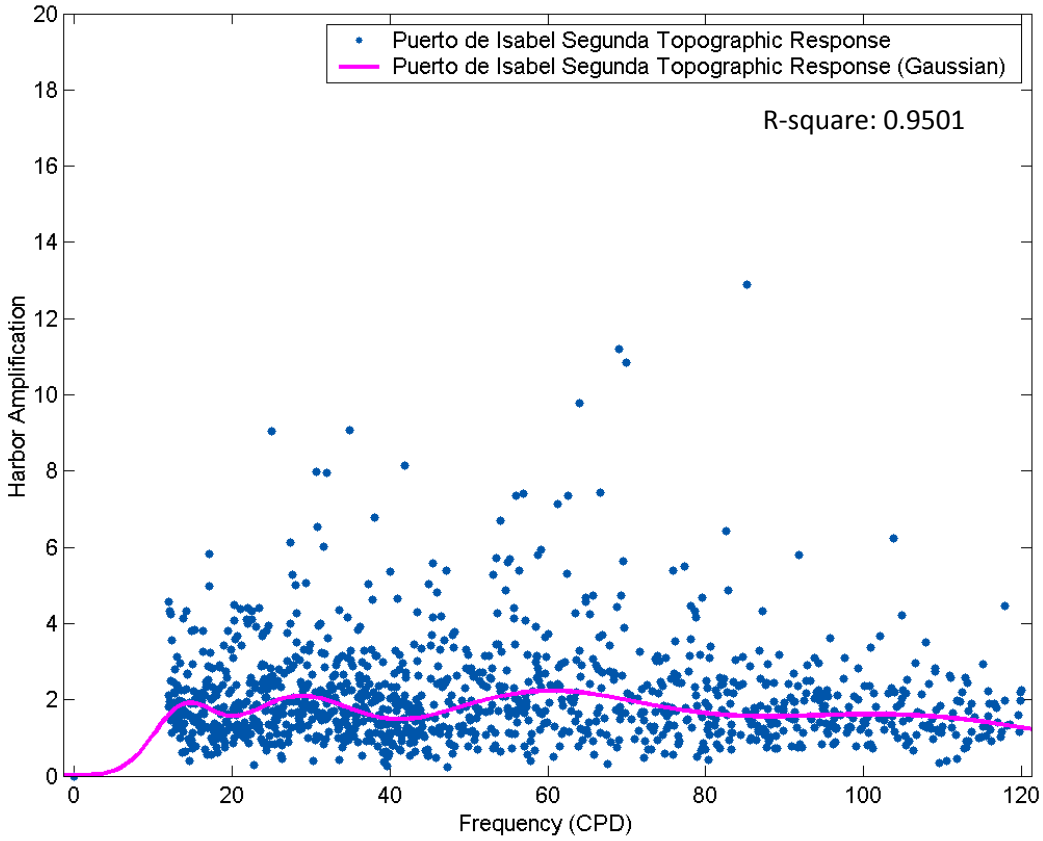
Puerto de Isabel Segunda Topographic Response
Puerto de Isabel Segunda Topographic Response (Gaussian)
R-square: 0.9501
Harbor Amplification
Frequency (CPD)
0
2
4
6
8
10
12
14
16
18
20
0
20
40
60
80
100
120

Figure 33

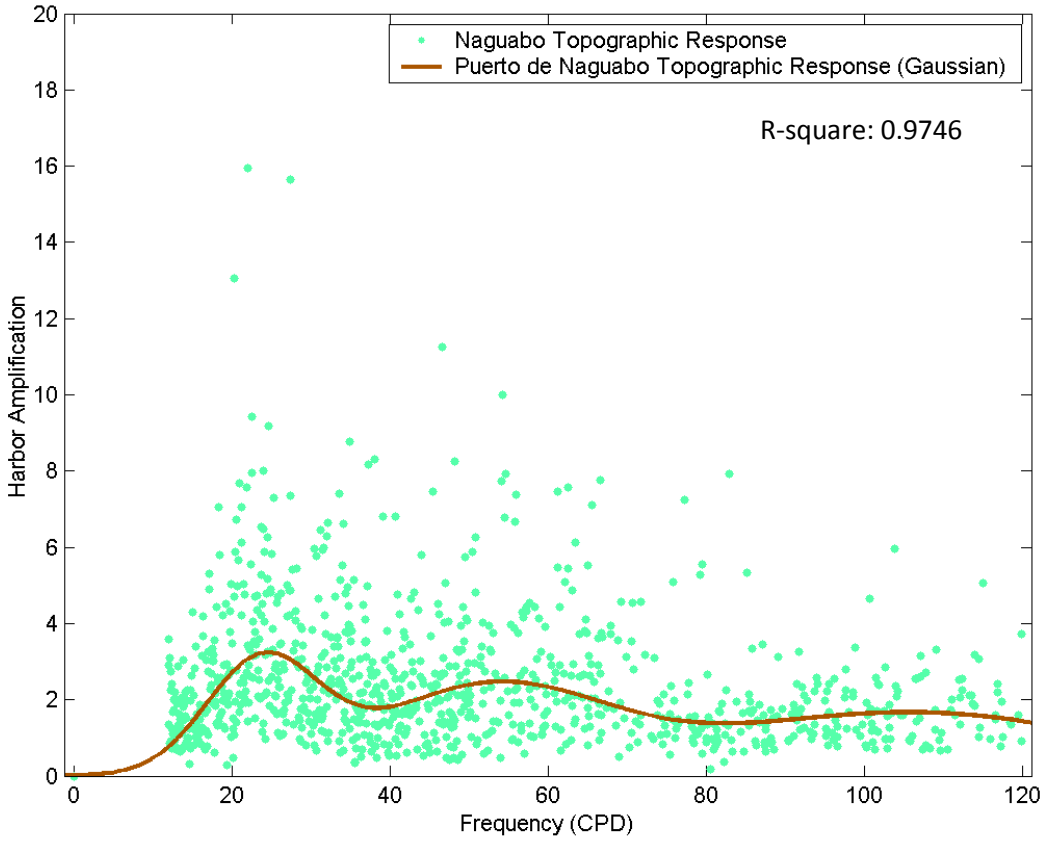
Naguabo Topographic Response
Puerto de Naguabo Topographic Response (Gaussian)
R-square: 0.9746
Harbor Amplification
Frequency (CPD)
0
2
4
6
8
10
12
14
16
18
20
0
20
40
60
80
100
120

Figure 34

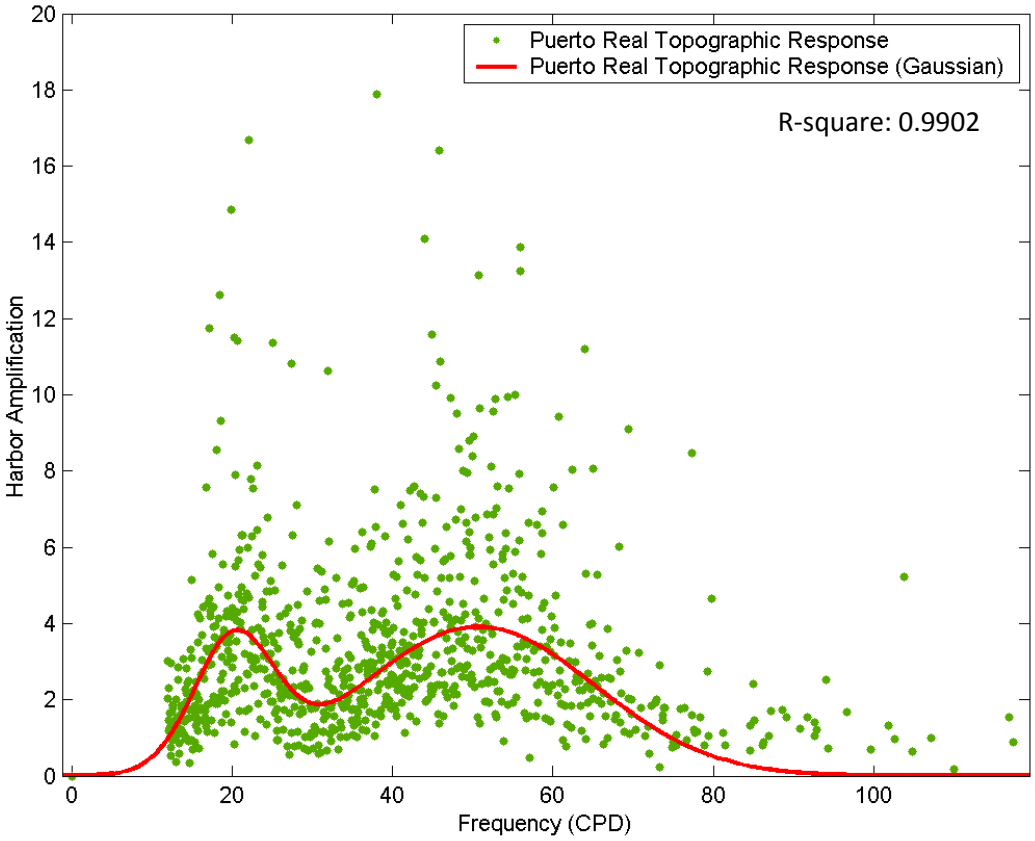
Puerto Real Topographic Response
Puerto Real Topographic Response (Gaussian)
R-square: 0.9902
Harbor Amplification
Frequency (CPD)
0
2
4
6
8
10
12
14
16
18
20
0
20
40
60
80
100

Figure 35

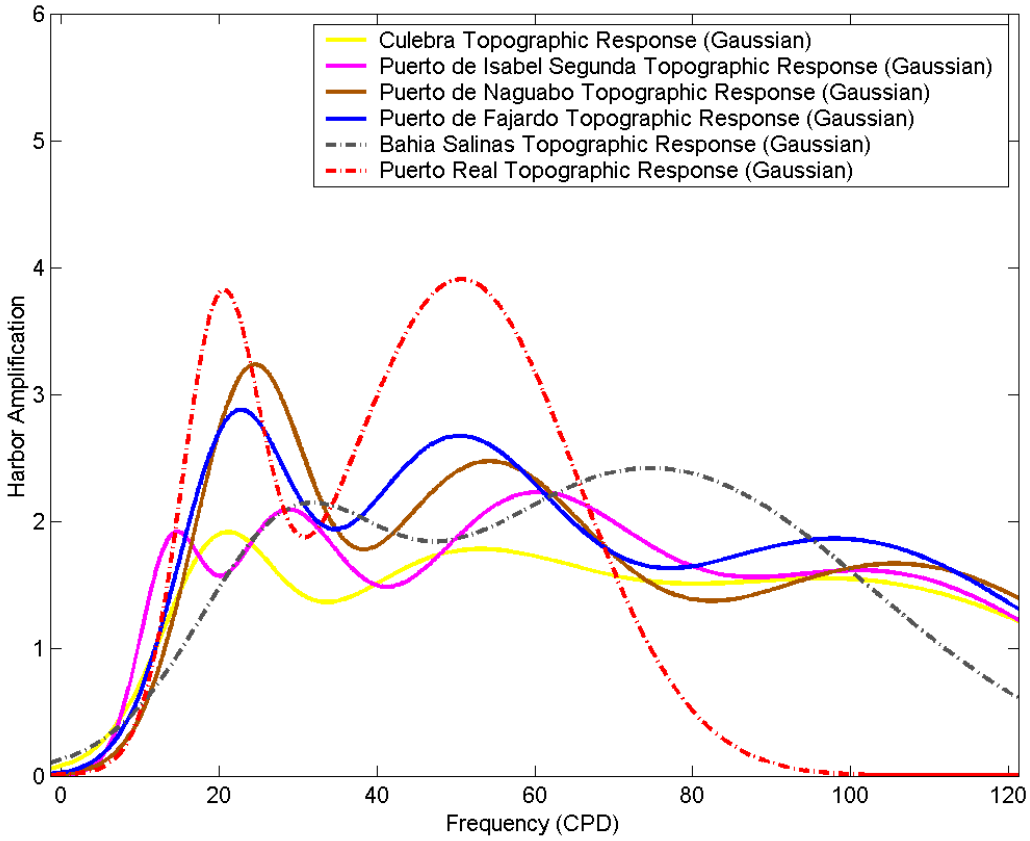

Figure 36

Bay or Harbor	Frequency (CPD)	Period (minutes)	Harbor Amplification
Bahia Salinas	32.1	44.9	2.2
Bahia Salinas	74.6	19.3	**2.4**
Culebra	21.1	68.3	1.9
Culebra	53.4	27.0	**1.8**
Puerto de Fajardo	22.9	62.8	**2.9**
Puerto de Fajardo	50.5	28.5	2.7
Puerto Isabel Segunda	14.7	98.0	1.9
Puerto Isabel Segunda	28.9	49.8	2.1
Puerto Isabel Segunda	60.4	23.8	**2.2**
Puerto de Naguabo	24.5	58.7	**3.2**
Puerto de Naguabo	54.4	26.5	2.5
Puerto Real	20.7	69.6	3.8
Puerto Real	50.6	28.5	**3.9**